

Chaotic imprints of dark matter in extreme mass-ratio inspirals

Mustapha Azreg-Aïnou,^{1,*} Mubasher Jamil,^{2,†} and Emmanuel N. Saridakis^{3,4,5,‡}

¹*Başkent University, Engineering Faculty, Bağlica Campus, 06790-Ankara, Türkiye*

²*School of Natural Sciences, National University of Sciences and Technology, H-12, Islamabad 44000, Pakistan*

³*Institute for Astronomy, Astrophysics, Space Applications and Remote Sensing,
National Observatory of Athens, 15236 Penteli, Greece*

⁴*Departamento de Matemáticas, Universidad Católica del Norte,
Avenida Angamos 0610, Casilla 1280 Antofagasta, Chile*

⁵*CAS Key Laboratory for Researches in Galaxies and Cosmology, School of Astronomy and Space Science,
University of Science and Technology of China, Hefei, Anhui 230026, China*

Extreme mass-ratio inspirals (EMRIs) are among the most powerful probes of strong-field gravity and of the environments surrounding supermassive compact objects. Motivated by the expected presence of dark matter near galactic centers, we investigate the emergence and gravitational-wave imprints of chaotic dynamics in EMRIs evolving in non-vacuum spacetimes. Within a unified dynamical framework, we analyze test-particle motion in a broad class of dark-matter-embedded geometries, including singular black holes, regular black holes, naked singularities, and Einstein-cluster configurations. We show that environmental perturbations generically break integrability in the strong-field regime, giving rise to chaotic motion whose onset, duration, and termination depend sensitively on horizon structure, core regularization, and matter distribution. Using the numerical Kludge approach, we demonstrate that chaotic trajectories produce systematic qualitative modifications of the emitted gravitational radiation, such as irregular amplitude modulation and loss of phase coherence, in contrast to the smooth, quasi-periodic waveforms generated by regular motion. Our results establish the robustness of chaos in environmentally perturbed EMRIs and provide a clear conceptual link between nonlinear orbital dynamics, spacetime structure, and observable gravitational-wave signatures.

I. INTRODUCTION

The direct detection of gravitational waves (GWs) by the LIGO and Virgo collaborations marked a turning point in modern astrophysics, placing gravitational-wave astronomy as a precision observational discipline [1, 2]. Gravitational waves provide a fundamentally new probe of the strong-field regime of gravity, granting direct access to dynamical spacetime phenomena that are either invisible or only indirectly inferred through electromagnetic observations. Among the most promising future sources in this context are *extreme mass-ratio inspirals* (EMRIs), consisting of a stellar-mass compact object spiraling into a supermassive compact object residing at the center of a galaxy.

EMRIs are expected to be primary targets of forthcoming space-based gravitational-wave detectors such as LISA [3], TianQin [4], and Taiji [5], operating in the millihertz frequency band. A defining feature of EMRIs is the exceptional duration of their signals, which can span $\mathcal{O}(10^4\text{--}10^6)$ orbital cycles before plunge. This extreme phase coherence renders EMRIs uniquely sensitive probes of spacetime geometry, enabling high-precision tests of general relativity [6], spacetime multipolar structure [7, 8], alternative theories of gravity [9–

11], and environmental effects surrounding supermassive compact objects [12, 13].

In realistic astrophysical settings, EMRIs do not evolve in vacuum. Supermassive black holes are expected to be embedded in complex environments that may include accretion disks [14], stellar clusters [15], magnetic fields [16], and dark-matter distributions [17, 18]. Although such effects are often treated as small perturbations, their cumulative impact over the long inspiral timescales characteristic of EMRIs can become dynamically significant. In particular, even weak environmental forces may break the integrability of geodesic motion, potentially leading to chaotic dynamics.

Chaos, characterized by sensitive dependence on initial conditions and the absence of most global constants of motion, is a generic feature of nonlinear Hamiltonian systems. In relativistic gravity, chaotic behavior has been identified in a wide range of contexts, including test-particle motion in deformed or perturbed black-hole spacetimes [19–21], compact-object binaries [22], and relativistic systems subject to external fields or non-vacuum matter configurations [23]. In the EMRI context, chaos is of particular interest because it can disrupt the quasi-periodic structure of the orbit and, in turn, leave distinctive imprints on the emitted gravitational radiation.

Motivated by astrophysical evidence for dark-matter concentrations near galactic centers [24, 25], numerous new exact solutions of black hole surrounded by dark matter have been reported in the literature [26–40]. Recent studies have explored the emergence of chaotic

* azreg@baskent.edu.tr

† mjamil@sns.nust.edu.pk

‡ msaridak@noa.gr

dynamics in EMRIs embedded in dark-matter environments. In particular, Refs. [41, 42] examined the motion of a stellar-mass object subject to an effective harmonic confinement and orbiting a Schwarzschild-like black hole surrounded by a Dehnen-type dark-matter halo. Using orbital projections, Poincaré sections, and Lyapunov indicators, these works demonstrated the existence of transitions from regular to chaotic motion controlled by the orbital energy and dark-matter parameters. Furthermore, qualitative differences between gravitational-wave signals generated by chaotic and non-chaotic trajectories were identified, including amplitude irregularities and spectral broadening [43]. It is interesting to note that both periodic as well as chaotic motions of neutral and charged particles around black holes have been frequently investigated in the literature [44–74].

Despite this progress, several key questions remain open. Existing analyses have focused almost exclusively on singular, Schwarzschild-like spacetimes and on specific realizations of dark-matter halos, leaving unexplored the extent to which chaotic dynamics and their gravitational-wave signatures are robust under changes in the underlying spacetime geometry. In particular, it remains unclear which aspects of chaos constitute universal features of environmentally perturbed EMRIs, and which depend sensitively on the presence of horizons, curvature singularities, or regularized cores. This issue is especially timely in view of the growing interest in *regular black holes*, which resolve central singularities while preserving asymptotic black-hole properties and arise in a variety of theoretical frameworks [75–99]. Since the near-horizon and interior structure of spacetime can directly influence orbital stability, capture mechanisms, and the duration of chaotic phases, a comparative analysis across different compact-object geometries is essential for assessing the physical relevance of chaos in realistic EMRI systems.

The purpose of the present work is to address these issues through a systematic and comparative investigation of chaotic dynamics in EMRIs embedded in dark-matter spacetimes. Adopting a unified dynamical framework based on horizon-regular coordinates, we analyze test-particle motion in a broad class of spherically symmetric geometries, including singular black holes, regular black holes, naked singularities, and Einstein-cluster configurations. Environmental effects are modeled through controlled external perturbations that explicitly break integrability, allowing us to isolate the onset, duration, and termination of chaotic motion across different spacetime realizations.

In addition to characterizing the orbital dynamics, we examine the gravitational-wave signatures of chaos using the numerical Kludge approach. While approximate in nature, this method is well suited for identifying robust qualitative imprints of chaotic motion on the emitted radiation. Our analysis demonstrates that chaos generically leads to irregular amplitude modulation and

loss of waveform coherence, and that these features persist across a wide range of spacetime geometries, albeit with important differences linked to horizon structure and core regularization.

The structure of the paper is as follows. In Section II we introduce the dynamical framework and describe the class of spherically symmetric spacetimes under consideration. Section III presents the diagnostics employed to identify chaotic behavior. In Section IV we perform a comparative analysis of chaotic dynamics across singular, regular, and horizonless dark-matter-embedded spacetimes. Section V is devoted to the corresponding gravitational-wave signatures and their qualitative imprints. Finally, Section VI summarizes our results and outlines directions for future work.

II. DYNAMICAL FRAMEWORK FOR EMRIS IN DARK MATTER SPACETIMES

In this section we establish the dynamical framework employed throughout the paper to describe the motion of a compact object in the vicinity of a massive central configuration embedded in a dark-matter environment. Our aim is to formulate the equations of motion in a manner that is sufficiently general to accommodate a wide class of spherically symmetric spacetimes, while remaining suitable for long-term numerical evolution in the strong-field regime.

A central requirement for the present analysis is the ability to follow the particle dynamics across regions where standard Schwarzschild-like coordinates become ill-behaved, such as near horizons or effective capture surfaces. For this reason, we adopt horizon-regular coordinate systems that allow for a continuous description of the motion and a transparent Hamiltonian formulation. This choice ensures that the onset of chaotic behavior, as well as its finite duration in spacetimes admitting capture, can be analyzed without coordinate artifacts.

Environmental effects associated with the surrounding dark-matter distribution are incorporated through effective external forces acting on the orbiting object. While simplified in form, this approach provides a controlled mechanism for breaking integrability and isolating the impact of non-vacuum environments on the orbital dynamics. The resulting framework serves as the basis for the chaos diagnostics discussed in the following section and for the construction of gravitational-wave signals analyzed later in the paper.

A. Spherically symmetric spacetimes and horizon-regular coordinates

We begin by considering a generic spherically symmetric and static (SSS) spacetime described by the line

element

$$ds^2 = -c^2 f(r) dt^2 + \frac{dr^2}{f(r)} + r^2 d\Omega^2, \quad (1)$$

where $d\Omega^2 = d\theta^2 + \sin^2\theta d\phi^2$ is the metric on the unit two-sphere. Such geometries encompass a wide class of black-hole and compact-object solutions, including Schwarzschild, regular black holes, and effective spacetimes describing dark-matter environments.

For the numerical investigation of particle dynamics, Schwarzschild-like coordinates are not suitable when the metric function $f(r)$ vanishes at a horizon. In order to regularize the metric at such locations, we introduce horizon-regular Painlevé-Gullstrand-type coordinates. For the metric (1), the transformation

$$\begin{aligned} c dt &= c dt_{\text{new}} - \frac{\sqrt{1-f(r)}}{f(r)} dr_{\text{new}}, \\ dr &= dr_{\text{new}}, \end{aligned} \quad (2)$$

brings the line element into the form

$$ds^2 = -c^2 f(r) dt^2 + 2c\sqrt{1-f(r)} dt dr + dr^2 + r^2 d\Omega^2, \quad (3)$$

where we have omitted the label “new” for simplicity.

More generally, we consider the SSS metric

$$ds^2 = -c^2 f(r) dt^2 + \frac{dr^2}{g(r)} + r^2 d\Omega^2. \quad (4)$$

In this case, a generalized Painlevé-Gullstrand coordinate transformation

$$\begin{aligned} c dt &= c dt_{\text{new}} - \frac{\sqrt{1-g(r)}}{\sqrt{f(r)g(r)}} dr_{\text{new}}, \\ dr &= dr_{\text{new}}, \end{aligned} \quad (5)$$

yields the horizon-regular metric

$$ds^2 = -c^2 f(r) dt^2 + 2c h(r) \sqrt{1-g(r)} dt dr + dr^2 + r^2 d\Omega^2, \quad (6)$$

where $h(r) \equiv \sqrt{f(r)/g(r)}$. If (4) describes a black hole solution, the functions f and g will have the same roots, and thus the function h is horizon-regular. Here again we have dropped the subscript “new”.

B. Effective Lagrangian and external environmental forces

We now consider the motion of a test particle of mass m confined to the equatorial plane $\theta = \pi/2$ of the spacetime (6). In the presence of environmental effects, modeled effectively through external forces, the dynamics is described by the Lagrangian

$$\begin{aligned} \mathcal{L} &= -mc \sqrt{c^2 f(r) - 2c h(r) \sqrt{1-g(r)} \dot{r} - \dot{r}^2 - r^2 \dot{\phi}^2} \\ &\quad - \frac{k_r}{2} (r - r_c)^2 - \frac{k_\phi r_h^2}{2} \phi^2, \end{aligned} \quad (7)$$

where overdots denote derivatives with respect to coordinate time t , and k_r , k_ϕ , and r_c are positive constants.

The last two terms in (7) represent effective harmonic potentials in the radial and angular directions. Such terms provide a simple phenomenological description of environmental perturbations, such as the effect of surrounding dark matter or stellar backgrounds, and have been widely employed in the literature as a controlled way to introduce non-integrability in otherwise symmetric systems. In the present work, these potentials are used solely as an effective modeling tool, and no claim is made regarding a detailed microscopic description of the underlying environment.

The validity of this effective description is restricted to regimes where the external forces act as small perturbations on the geodesic motion, allowing one to isolate and study qualitative features of the resulting dynamics.

C. Equations of motion and conserved quantities

We now proceed to derive the equations of motion associated with the Lagrangian (7). The corresponding canonical momenta and Hamiltonian structure provide a convenient formulation of the dynamics, allowing for a systematic investigation of conserved quantities and integrability properties. The canonical momenta conjugate to r and ϕ are obtained as

$$p_r = \frac{\partial \mathcal{L}}{\partial \dot{r}} = \frac{mc[\dot{r} + c h(r) \sqrt{1-g(r)}]}{\sqrt{c^2 f(r) - 2c h(r) \sqrt{1-g(r)} \dot{r} - \dot{r}^2 - r^2 \dot{\phi}^2}}, \quad (8)$$

$$p_\phi = \frac{\partial \mathcal{L}}{\partial \dot{\phi}} = \frac{mcr^2 \dot{\phi}}{\sqrt{c^2 f(r) - 2c h(r) \sqrt{1-g(r)} \dot{r} - \dot{r}^2 - r^2 \dot{\phi}^2}}. \quad (9)$$

The conserved energy of the test mass m is given by

$$\begin{aligned} E &= p_r \dot{r} + p_\phi \dot{\phi} - \mathcal{L} \\ &= \frac{mc^2 [c f(r) - h(r) \sqrt{1-g(r)} \dot{r}]}{\sqrt{c^2 f(r) - 2c h(r) \sqrt{1-g(r)} \dot{r} - \dot{r}^2 - r^2 \dot{\phi}^2}} \\ &\quad + \frac{k_r}{2} (r - r_c)^2 + \frac{k_\phi r_h^2}{2} \phi^2, \end{aligned} \quad (10)$$

which after eliminating $(\dot{r}, \dot{\phi})$ in terms of (p_r, p_ϕ) , reads

$$\begin{aligned} E &= -c h(r) \sqrt{1-g(r)} p_r + \frac{c h(r) \sqrt{(c^2 m^2 + p_r^2) r^2 + p_\phi^2}}{r} \\ &\quad + \frac{k_r}{2} (r - r_c)^2 + \frac{k_\phi r_h^2}{2} \phi^2. \end{aligned} \quad (11)$$

The equations of motion can be written in first-order Hamiltonian form as

$$\dot{r} = -c h(r) \sqrt{1-g(r)} + \frac{c h(r) r p_r}{\sqrt{(c^2 m^2 + p_r^2) r^2 + p_\phi^2}}, \quad (12)$$

$$\dot{\phi} = \frac{c h(r) p_{\phi}}{r \sqrt{(c^2 m^2 + p_r^2) r^2 + p_{\phi}^2}}, \quad (13)$$

$$\begin{aligned} \dot{p}_r = c h(r) & \left[-\frac{g'(r) p_r}{2\sqrt{1-g(r)}} + \frac{p_{\phi}^2}{r^2 \sqrt{(c^2 m^2 + p_r^2) r^2 + p_{\phi}^2}} \right] \\ & + \frac{c h'(r) [r p_r \sqrt{1-g(r)} - \sqrt{(c^2 m^2 + p_r^2) r^2 + p_{\phi}^2}]}{r} \\ & - k_r (r - r_c), \quad (14) \end{aligned}$$

$$\dot{p}_{\phi} = -k_{\phi} r_h^2 \phi. \quad (15)$$

It is worth mentioning that in the case where $g(r) = f(r)$, that is $h(r) = \sqrt{f(r)/g(r)} \equiv 1$, the second line in (14) vanishes identically and all equations of motion reduces to those of the case $g(r) = f(r)$.

In the numerical analysis presented below, we adopt units in which $M = 1 = c = G$, while the mass of the orbiting compact object is fixed to $m = 10^{-5}$. The outer horizon radius is denoted by r_h , and for the external potentials we choose $k_r = 100$, $k_{\phi} = 25$, and $r_c = 4$. In cases where the central object corresponds to a naked singularity or a regular compact object without a horizon, r_h in (7) is replaced by the corresponding characteristic radius of the object.

III. DIAGNOSTICS OF CHAOTIC DYNAMICS

Chaotic dynamics in relativistic systems is characterized by sensitive dependence on initial conditions and by the breakdown of long-term predictability, even when the underlying equations of motion are fully deterministic. In the context of extreme mass-ratio inspirals embedded in non-vacuum or non-integrable environments, chaos may arise from the interplay between strong-field gravity, external perturbations, and environmental structure. Since no single diagnostic provides a complete characterization of chaotic behavior, it is essential to employ a combination of complementary tools that probe both the geometrical and dynamical aspects of the motion.

In this section, we introduce and apply a set of standard diagnostics of chaos adapted to the present framework. These include projections of orbital motion and Poincaré sections, which offer direct insight into phase-space structure, as well as criteria for identifying transitions between regular and chaotic regimes. We place particular emphasis on the finite-time nature of chaotic behavior in strong-field spacetimes, where capture by a horizon or singularity generically limits the duration of chaotic motion. The diagnostics presented here form the basis for the comparative analysis of different spacetime geometries in Section IV and for the investigation of gravitational-wave signatures discussed in Section V.

A. Orbital projections and Poincaré sections

A first qualitative characterization of the orbital dynamics is obtained by examining projections of particle trajectories onto the equatorial plane $\theta = \pi/2$. In integrable or quasi-integrable regimes, such projections exhibit smooth, regular patterns corresponding to bounded and recurrent motion. In contrast, chaotic trajectories typically generate irregular, densely populated regions in configuration space, reflecting the sensitive dependence on initial conditions and the absence of additional constants of motion beyond those imposed by symmetries.

While orbital projections provide an intuitive visualization of the motion, a more refined diagnostic is furnished by Poincaré sections. These are constructed by recording the phase-space coordinates of the particle each time the trajectory intersects a prescribed surface of section. In the present analysis, we employ sections in the (r, p_r) plane, evaluated at fixed values of the conjugate angular.

For regular motion, Poincaré sections consist of closed invariant curves, indicating that the dynamics is confined to tori in phase space. Chaotic motion, on the other hand, is characterized by the progressive destruction of such invariant structures and the appearance of scattered points that fill extended regions of the section. Intermediate configurations, where invariant curves coexist with stochastic layers, signal the onset of chaos and the breakdown of integrability.

B. Transition to chaos and finite-time chaotic behavior

In the systems under consideration, the transition from regular to chaotic dynamics does not necessarily occur abruptly. Instead, particle motion often displays a mixed character, whereby initially regular trajectories evolve into chaotic ones after a finite time interval. Such behavior is commonly encountered in non-integrable Hamiltonian systems and is particularly relevant in relativistic settings where strong-field effects become significant.

A salient feature of the present framework is the emergence of finite-time chaos. In this case, the motion exhibits clear chaotic signatures, such as stochastic Poincaré sections and irregular orbital projections, over a limited time span, before the trajectory terminates due to capture by the central object. This phenomenon is especially pronounced in regions close to horizons or singularities, where the effective potential and spacetime curvature vary rapidly and amplify nonlinear effects.

Near-horizon dynamics plays a crucial role in this context. As the particle approaches the strong-field region, small perturbations in the initial conditions can lead to markedly different orbital evolutions, enhancing sensitivity and promoting chaotic behavior. Nevertheless, since the inspiraling object ultimately crosses the

horizon or reaches a singularity, chaos manifests itself only over a finite duration. For this reason, the relevant notion is not asymptotic chaos in the mathematical sense, but rather finite-time chaotic dynamics with direct physical implications for the orbital evolution.

In this work, we adopt a practical operational definition of chaos based on the combined use of orbital projections and Poincaré sections. Trajectories are classified as chaotic when their projections lose regular structure and the corresponding Poincaré sections exhibit scattered, non-toroidal distributions over the available phase-space region. This criterion allows for a consistent identification of chaotic behavior across different spacetime geometries and parameter choices, and it is particularly well suited for systems where the motion terminates after a finite time.

IV. DARK-MATTER-EMBEDDED SPACETIMES: A COMPARATIVE ANALYSIS OF CHAOTIC DYNAMICS

In this section we present the core comparative analysis of chaotic dynamics in extreme mass-ratio inspirals evolving within dark-matter-embedded spacetimes. Our central aim is to determine which features of chaotic motion are generic consequences of environmental perturbations in the strong-field regime, and which depend sensitively on the geometric structure of the underlying spacetime.

To address this question systematically, we examine representative geometries that span a wide spectrum of physically distinct configurations: singular black holes surrounded by dark-matter halos, regular black holes with non-singular cores, naked singularities, and Einstein-cluster solutions. This classification allows us to isolate the role played by horizon structure, curvature singularities, and core regularization in governing the onset, persistence, and termination of chaotic motion.

A unified diagnostic framework is employed throughout, based on orbital projections and Poincaré sections applied consistently across all spacetimes. By maintaining the same dynamical setup and perturbative structure, we ensure that differences in chaotic behavior can be attributed directly to geometric properties rather than to modeling artifacts. In particular, special attention is devoted to the finite-time nature of chaos in geometries admitting capture, in contrast with the more extended chaotic phases that may arise in regular configurations.

This section therefore serves a dual purpose. First, it establishes chaos as a structurally robust feature of EMRI dynamics in non-vacuum environments. Second, it clarifies how spacetime geometry and dark-matter parameters modulate its manifestation, thereby providing the physical foundation for the gravitational-wave analysis presented in the next section.

A. Singular black holes in dark matter halos

We begin with singular black-hole geometries immersed in dark-matter distributions. These configurations represent the closest extensions of the Schwarzschild solution and thus provide a natural reference point for assessing the impact of environmental perturbations on orbital stability. By first analyzing spacetimes that retain a central curvature singularity, we establish a baseline against which the effects of core regularization and horizon modification can later be contrasted.

1. Zhao-type dark-matter-embedded black holes

As a first example, we consider a black hole immersed in a dark-matter halo described by the Zhao density profile [100]

$$\rho(r) = \rho_s \frac{(r/r_s)^{\mu-3}}{[1 + (r/r_s)^\nu]^{(\mu+\alpha)/\nu}}, \quad (16)$$

where r_s is a characteristic length scale, ρ_s denotes the central density, and (α, μ, ν) are dimensionless parameters. In what follows we restrict ourselves to the representative choice $(\alpha, \mu, \nu) = (1, 3, 2)$, which leads to a well-behaved density profile at large radii.

The corresponding spacetime geometry is assumed to take the form

$$ds^2 = -c^2 f(r) dt^2 + \frac{dr^2}{1 - \frac{2Gm(r)}{c^2 r}} + r^2 d\Omega^2, \quad (17)$$

with

$$f(r) = 1 - \frac{2Gm(r)}{c^2 r}, \quad (18)$$

where $m(r)$ is the enclosed mass function determined by the dark-matter distribution. In Appendix A we provide an outlined derivation of the metric function $f(r)$, which takes the form

$$m(r) = M - \frac{2\pi r_s^4 \rho_s r}{r^2 + r_s^2} + 2\pi r_s^3 \rho_s \arctan\left(\frac{r}{r_s}\right), \quad (19)$$

$$f(r) = 1 - \frac{2GM}{c^2 r} + \frac{4\pi G r_s^4 \rho_s}{c^2 (r^2 + r_s^2)} - \frac{4\pi G r_s^3 \rho_s}{c^2 r} \arctan\left(\frac{r}{r_s}\right), \quad (20)$$

where the constant of integration M is the mass of the central object (which, as we shall see, is a BH).

Although the Ricci scalar remains finite throughout the spacetime, the Kretschmann invariant diverges at the origin, indicating the presence of a curvature singularity. Furthermore, the equation $f(r) = 0$ admits positive real roots, corresponding to the existence of an

event horizon. In the limit $\rho_s \rightarrow 0$, the solution continuously reduces to the Schwarzschild black hole, confirming the singular black-hole character of the spacetime.

Concerning the distribution of dark matter inside the horizon, we note that there is currently no observational evidence excluding its presence in this region. One may either assume that the dark-matter halo extends smoothly from spatial infinity down to the singularity, or alternatively introduce a matching to an interior vacuum solution at a finite radius. Since our focus lies on the dynamics of massive particles in the vicinity of the event horizon, we adopt the former assumption for simplicity.

Within this background, orbital motion exhibits both regular and chaotic regimes, depending on the system parameters (see Fig. 1). As discussed in Section III, chaotic behavior is identified through irregular orbital projections and stochastic Poincaré sections, while regular motion is associated with smooth, quasi-periodic structures.

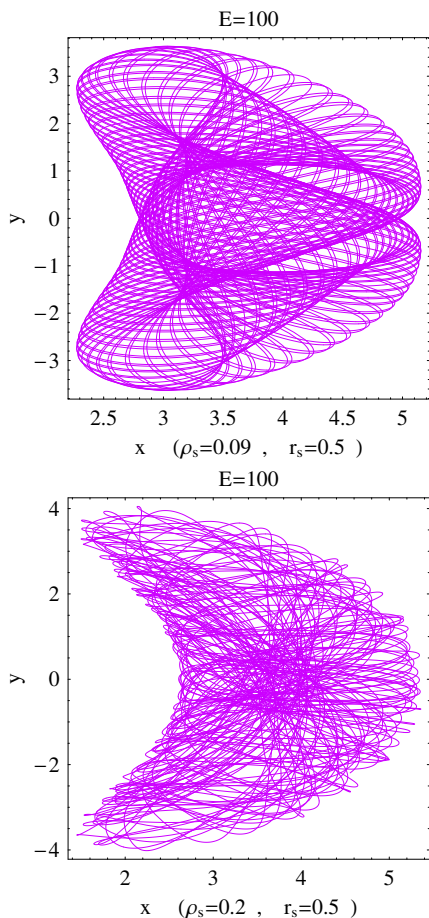


FIG. 1. Orbital projections onto the equatorial plane ($\theta = \pi/2$) in the spacetime described by metric (19), for $E = 100$ and $r_s = 0.5$. The integration interval is $0 \leq t \leq 6000$ (in units of M). Upper panel: Non-chaotic motion for $\rho_s = 0.09$, corresponding to horizon radius $r_h = 2.16$. Lower panel: Chaotic motion for $\rho_s = 0.2$, corresponding to $r_h = 2.36$. Units $G = c = M = 1$ are adopted.

2. Bronnikov-type singular configurations

As a second example of a singular black hole embedded in a dark-matter environment, we consider the spacetime introduced in [101, 102], characterized by the metric function

$$f(r) = 1 - \frac{2GM}{c^2 r} + \frac{8\pi G r_s^4 \rho_s}{c^2 r (r^3 + r_s^3)^{1/3}}. \quad (21)$$

This geometry also possesses a central curvature singularity and admits at least one event horizon for appropriate parameter choices. Note that if $M = 4\pi r_s^3 \rho_s$, the curvature and Kretschmann scalars are finite for all r and the solution is regular (compare with Eq. (25) of [101]).

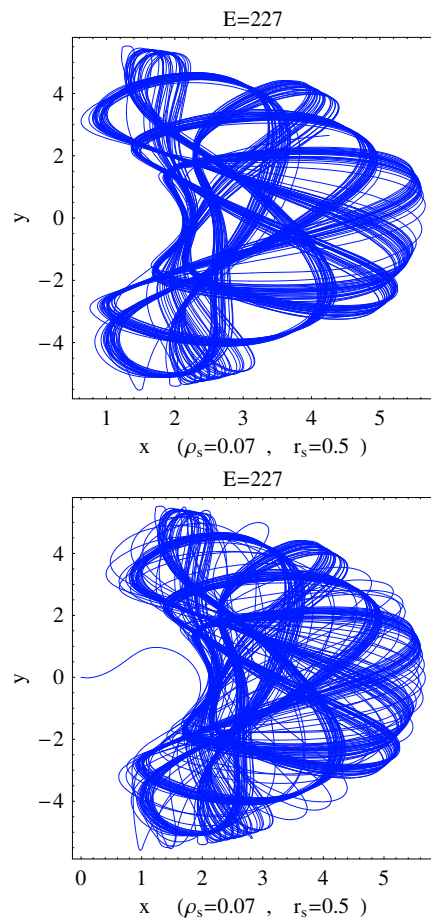


FIG. 2. Orbital projections onto the equatorial plane ($\theta = \pi/2$) in the Bronnikov-type geometry (21), for $E = 227$, $\rho_s = 0.07$, and $r_s = 0.5$. The corresponding horizon radius is $r_h = 1.94$. Upper panel: Chaotic trajectory integrated over $0 \leq t \leq 5000$ (in units of M), terminating at $(x, y) = (4.26, 2.65)$ prior to plunge. Lower panel: Chaotic trajectory integrated over $0 \leq t \leq 5800$, ultimately ending at the central singularity $(x, y) = (0, 0)$. Units $G = c = M = 1$ are used.

Compared to the Zhao-type configuration, the Bronnikov-type spacetime exhibits a richer dynamical

structure. For identical values of the external-force parameters and particle mass, particle trajectories often display a transition from initially regular motion to chaotic behavior before ultimately terminating at the singularity (see Fig. 2 and Fig. 3). Such mixed dynamics is indicative of non-integrability and is consistent with the finite-time chaotic behavior discussed in Section III.

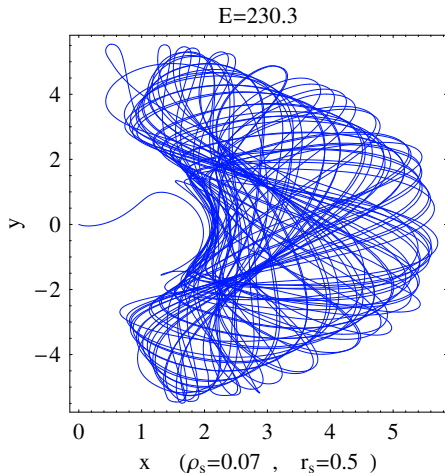


FIG. 3. Orbital projection onto the equatorial plane ($\theta = \pi/2$) in the Bronnikov-type spacetime (21), for $E = 230$, $\rho_s = 0.07$, and $r_s = 0.5$. The corresponding horizon radius is $r_h = 1.94$. The trajectory is integrated over the interval $0 \leq t \leq 2000$ (in units of M). Units $G = c = M = 1$ are adopted.

The enhanced complexity of the phase-space structure in this case suggests that the detailed form of the dark-matter-induced modification to the metric can significantly influence the onset and duration of chaotic motion. Nevertheless, the presence of a singular core and an event horizon ensures that chaotic behavior remains transient, as trajectories eventually fall into the central singularity.

3. Qualitative comparison

Both singular black-hole configurations considered above share several common features. In particular, the presence of an event horizon and a central singularity leads to finite-time chaotic dynamics, with chaos typically emerging in the strong-field region before capture. At the same time, quantitative differences in the transition to chaos and the extent of chaotic regions in phase space highlight the sensitivity of the dynamics to the detailed spacetime structure induced by the dark-matter distribution.

These singular spacetimes therefore provide a useful reference class for assessing the robustness of chaotic behavior, against which regular black holes and horizonless configurations will be compared in the following subsections.

B. Regular black holes and the role of core regularization

Regular black hole geometries provide a particularly instructive setting for probing the impact of core regularization on chaotic dynamics. By removing the central curvature singularity while preserving the existence of an effective gravitational potential, such spacetimes allow one to disentangle the effects of strong-field gravity from those associated with singular behavior. In this context, regular cores are expected to modify both the onset and the temporal development of chaos, potentially allowing for extended or smoother transitions between regular and chaotic motion.

In the following, we focus on a representative regular black hole model and analyze how core regularization influences the structure of phase space and the associated orbital dynamics in the presence of environmental perturbations.

1. Simpson-Visser regular black holes

We now turn to regular black-hole spacetimes, namely configurations in which curvature singularities are resolved while the exterior geometry remains asymptotically Schwarzschild-like. Such spacetimes provide an instructive arena for assessing the impact of a regular core on the emergence and properties of chaotic motion.

As a representative example, we consider the regular black hole proposed by Simpson and Visser [99], described by the line element

$$ds^2 = -c^2 \left(1 - \frac{2GM}{c^2 \sqrt{r^2 + a^2}} \right) dt^2 + \frac{dr^2}{1 - \frac{2GM}{c^2 \sqrt{r^2 + a^2}}} + (r^2 + a^2) d\Omega^2, \quad (22)$$

where M is the mass parameter and a is a length scale that controls the regularization of the central region. In the limit $a \rightarrow 0$, the metric smoothly reduces to the Schwarzschild solution, while for finite a the spacetime is free of curvature singularities.

For our numerical analysis we have two options, either we work with (22) where $g = f$ and

$$\mathcal{L} = -mc \sqrt{c^2 f(r) - 2c \sqrt{1 - f(r)} \dot{r} - \dot{r}^2 - (r^2 + a^2) \dot{\phi}^2} - \frac{k_r}{2} (r - r_c)^2 - \frac{k_\phi r_h^2}{2} \phi^2,$$

or we bring metric (22) to the form (4). We choose the second option and use \mathcal{L} as given in (7). This is done upon introducing the new radial variable $r_{\text{new}} =$

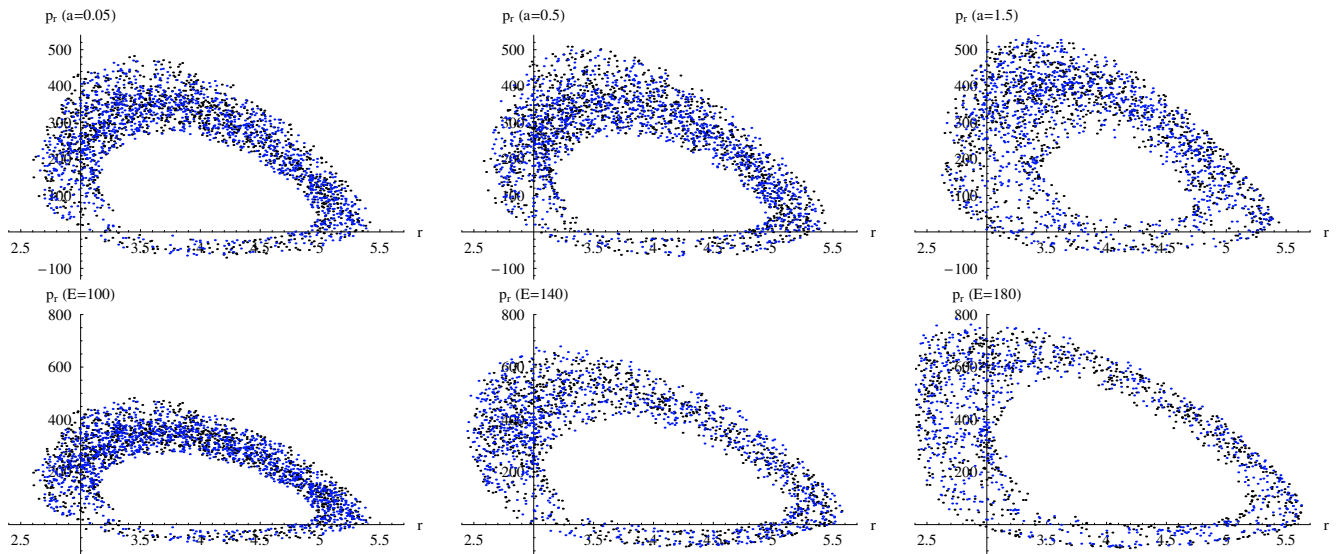


FIG. 4. Poincaré sections constructed at $\phi = 0.5$ for the Simpson-Visser spacetime (22). Initial conditions are $(r(0), \phi(0), p_r(0)) = (3.0, 0.1, 0.1)$ (black points) and $(3.0, -0.1, -0.1)$ (blue points). The integration interval is $0 \leq t \leq 5 \times 10^4$ (in units of M). Upper panel: Dependence on the regularization parameter a for fixed $E = 100$ and $a = 0.05, 0.5, 1.5$. Lower panel: Dependence on the orbital energy E for fixed $a = 0.05$ and $E = 100, 140, 180$. Units $G = c = M = 1$ are adopted.

$\sqrt{r^2 + a^2}$. The new functions g , f , and h read

$$g(r) = \frac{(c^2 r - 2GM)(r^2 - a^2)}{c^2 r^3}, \quad r > a, \quad (23)$$

$$f(r) = \frac{(c^2 r - 2GM)}{c^2 r}, \quad (24)$$

$$h(r) = \sqrt{\frac{f}{g}} = \frac{r}{\sqrt{r^2 - a^2}}, \quad (25)$$

where we dropped the subscript “new”.

The presence of the regular core modifies the strong-field structure of the spacetime in comparison with the singular black holes discussed in subsection IV A. In particular, curvature invariants remain finite throughout the geometry, and the effective gravitational potential experienced by massive particles differs significantly in the innermost region. Depending on the value of the parameter a , the spacetime may describe either a regular black hole with an event horizon or a horizonless compact object.

When embedded in a dark-matter environment and supplemented by external perturbations, particle motion in the Simpson-Visser spacetime exhibits both regular and chaotic regimes. However, in contrast to singular black holes, the absence of a central curvature divergence alters the termination of trajectories and the manifestation of finite-time chaos. As a result, chaotic behavior may persist over longer time intervals and display qualitative differences in phase-space structure, reflecting the influence of the regular core (see Fig. 4).

These features make regular black-hole geometries particularly suitable for disentangling universal aspects of chaotic dynamics from those that depend sensitively

on the presence of singularities. A systematic comparison with singular and horizonless configurations will be carried out in the following subsections.

2. Effect of regular core on chaos onset

The replacement of a central curvature singularity by a regular core has a direct impact on the onset and development of chaotic dynamics. In singular black-hole spacetimes, chaotic behavior typically emerges in the strong-field region and is intrinsically finite in duration, as particle trajectories eventually terminate at the singularity after crossing the event horizon. In such cases, chaos manifests itself primarily as a transient phenomenon associated with near-horizon dynamics.

In regular black-hole geometries, the situation is qualitatively different. Since curvature invariants remain finite throughout the spacetime, the effective potential experienced by the orbiting particle does not diverge in the central region. As a consequence, trajectories are not forcibly terminated by a singularity, allowing chaotic motion to persist over longer time intervals. This extended dynamical evolution facilitates a clearer manifestation of chaotic features in phase space, including prolonged stochastic behavior and more developed mixing in Poincaré sections.

Furthermore, the absence of a singular core modifies the conditions under which chaos is triggered. In particular, the transition from regular to chaotic motion tends to occur more smoothly, with chaotic behavior often setting in at later stages of the evolution compared to singular configurations. This indicates that, while the pres-

ence of an event horizon continues to play a role in shaping strong-field dynamics, the detailed structure of the spacetime interior can significantly influence the sensitivity of particle motion to perturbations.

Overall, these findings suggest that regular cores act to moderate the abruptness of chaos onset and extend the temporal window over which chaotic dynamics can develop. This behavior highlights the importance of distinguishing between horizon-related effects and those associated with the central structure of the spacetime, a point that will be further clarified in the comparative discussion of the following sections.

C. Naked singularities and Einstein-cluster configurations

We now turn to spacetimes describing compact objects embedded in dark-matter distributions that give rise to naked singularities or composite configurations involving Einstein clusters. These geometries provide a qualitatively different arena for studying chaotic dynamics, as they may lack an event horizon or exhibit piecewise structures that interpolate between vacuum and matter-dominated regions.

1. Metric construction and general properties

We start with configurations that depart qualitatively from the black-hole geometries considered so far. In particular, we investigate horizonless spacetimes sourced by an anisotropic dark-matter distribution, which may describe either naked-singularity configurations or Einstein-cluster solutions depending on the parameter regime. These geometries provide a useful laboratory for assessing how the absence of an event horizon modifies the onset and evolution of chaotic motion.

In Appendix B we outline the derivation of the corresponding metric functions $f(r)$ and $g(r)$ within general relativity. The spacetime under consideration is characterized by two length scales,

$$r_+ = \frac{2GM}{c^2}, \quad r_- = \frac{4\pi r_s^4 \rho_s}{M}, \quad (26)$$

which encode the contribution of the central mass and the surrounding dark-matter distribution, respectively. The metric can be written in the generic spherically symmetric form (4), with the explicit expressions for $f(r)$ and $g(r)$ depending on the relative magnitude of r_- and r_+ .

The matter source corresponds to an Einstein cluster, characterized by vanishing radial pressure and non-zero tangential pressure, while satisfying the weak energy condition. This provides a physically consistent realization of an extended dark-matter distribution stretching from a finite radius to spatial infinity.

2. Case $r_- < r_+$: naked singularity configurations

We consider the parameter regime $r_- < r_+$, in which the dark-matter contribution remains subdominant relative to the central mass scale. In this case the geometry does not admit an event horizon shielding the central curvature singularity, and the spacetime represents a naked singularity immersed in an extended dark-matter distribution. This configuration provides an instructive contrast with the black-hole cases discussed previously, since the absence of a horizon can significantly modify the late-time evolution of chaotic trajectories.

The corresponding metric functions take the form

$$\begin{aligned} r_+ &= \frac{2GM}{c^2}, & r_- &= \frac{4\pi r_s^4 \rho_s}{M}, & r_- &< r_+ \\ m(r) &= M \left(1 + \frac{r_-}{r_+}\right) - M \frac{r_-}{r}, \\ f(r) &= \left(1 - \frac{r_+}{r}\right)^{\frac{r_+}{r_+ - r_-}} \left(1 - \frac{r_-}{r}\right)^{-\frac{r_-}{r_+ - r_-}}, \\ g(r) &= \left(1 - \frac{r_+}{r}\right) \left(1 - \frac{r_-}{r}\right) = \frac{(r - r_+)(r - r_-)}{r^2}, \end{aligned} \quad (27)$$

where M denotes the central mass and

$$\frac{Mr_-}{r_+} = \int_{r_+}^{\infty} 4\pi r^2 \rho(r) dr$$

is the total mass contribution from the dark-matter distribution (with $\rho = m'(r)/(4\pi r^2) = r_s^4 \rho_s / r^4$). The mass function $m(r)$ is defined through $g(r) = 1 - 2Gm(r)/(c^2 r)$.

The radial pressure vanishes identically ($\kappa \equiv 8\pi G/c^4$)

$$\kappa p_r = \frac{c^2 r - 2Gm(r)}{c^2 r^2} \frac{f'(r)}{f(r)} - \frac{2Gm(r)}{c^2 r^3} \equiv 0, \quad (28)$$

and the tangential pressure is given by

$$p_t = \frac{c^2 Gm(r) m'(r)}{8\pi r^2 [c^2 r - 2Gm(r)]} > 0. \quad (29)$$

Thus, this dark matter configuration represents an Einstein cluster. Since

$$\begin{aligned} \rho(r) &= \frac{m'(r)}{4\pi r^2} = \frac{Mr_-}{4\pi r^4} > 0, \\ \rho(r) + \frac{p_r}{c^2} &> 0, \\ \rho(r) + \frac{p_t}{c^2} &> 0, \end{aligned} \quad (30)$$

we conclude that the Weak Energy Condition (WEC) is satisfied.

Particle dynamics in this background exhibits finite-time chaotic behavior (see Fig. 5). Trajectories may display chaotic signatures over an extended period, characterized by irregular orbital projections and stochastic Poincaré sections, before ultimately terminating at the

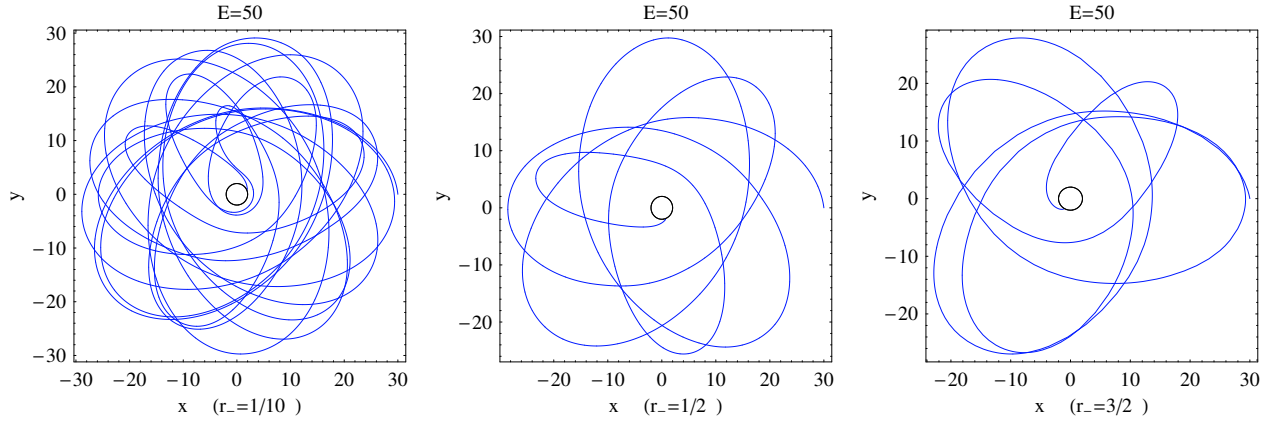


FIG. 5. *Orbital projections onto the equatorial plane ($\theta = \pi/2$) in the spacetime (27), corresponding to the case where the central mass M exceeds the dark-matter mass contribution ($M > M_{\text{DM}}$). In this regime, the naked singularity is located at $r = r_+$. The trajectories are shown for $E = 50$ and $r_- = 0.1, 0.5, 1.5$. Units $G = c = M = 1$ are adopted.*

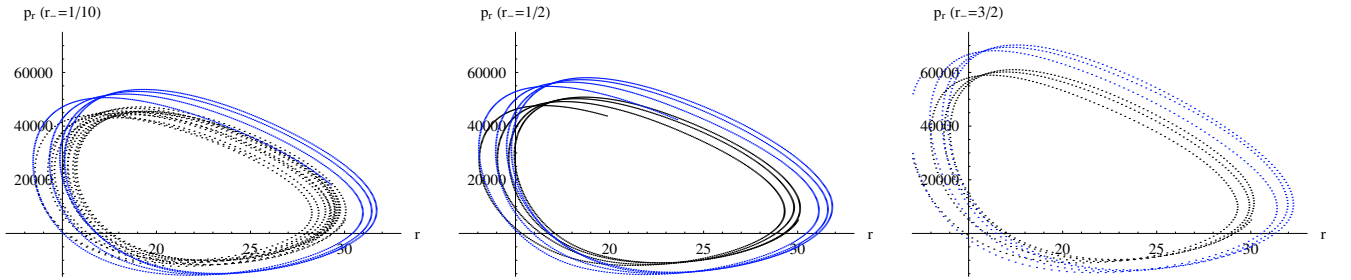


FIG. 6. *Poincaré sections in the (r, p_r) plane for the spacetime (27), corresponding to the regime where the central mass exceeds the dark-matter contribution ($M > M_{\text{DM}}$), with the naked singularity located at $r = r_+$. The parameters are $E = 50$, $r_+ = 2GM/c^2 = 2$, and $r_- = 0.1, 0.5, 1.5$, illustrating the effect of increasing $r_s^4 \rho_s$ for fixed m . Initial conditions are $(r(0), \phi(0), p_r(0)) = (30, 0, 5000)$ (black points) and $(30, 0, -5000)$ (blue points). Units $G = c = M = 1$ are adopted.*

naked singularity (see Fig. 6). The absence of an event horizon implies that capture occurs directly at the singularity, rendering the chaotic phase intrinsically transient.

The duration and intensity of chaotic motion depend sensitively on the parameters controlling the dark-matter distribution. In particular, increasing the scale radius of the Einstein cluster tends to enhance the complexity of phase-space structures, as reflected in the increased population of both inner and outer regions of the Poincaré sections prior to capture.

3. Case $r_- > r_+$: Einstein cluster surrounding a black hole

In the opposite regime, $r_- > r_+$, the dark-matter contribution equals or exceeds that of the central mass. The resulting spacetime describes a Schwarzschild black hole surrounded by an Einstein cluster extending from $r = r_-$ to spatial infinity. In this case, the metric function $g(r)$ remains strictly positive outside the horizon, while the interior region $0 < r < r_-$ is described by the

Schwarzschild solution.

$$\begin{aligned}
 r_+ &= \frac{2GM}{c^2}, & r_- &= \frac{4\pi r_s^4 \rho_s}{M}, & r_- &> r_+ \\
 m(r) &= 2M - M \frac{r_-}{r}, \\
 f &= \sqrt{g} \exp \left\{ \sqrt{\frac{r_+}{r_- r_+}} \left[\arctan \left(\frac{r - r_+}{\sqrt{r_+(r - r_+)}} \right) - \frac{\pi}{2} \right] \right\}, \\
 g(r) &= 1 - \frac{2Gm(r)}{c^2 r} = \frac{(r - r_+)^2 + r_+(r_- - r_+)}{r^2} > 0, \tag{31}
 \end{aligned}$$

where M is the central mass of the naked singularity, and the contribution to the total mass from the DM is also $M = \int_{r_-}^{\infty} 4\pi r^2 \rho(r) dr$ [with $\rho = m'(r)/(4\pi r^2) = r_s^4 \rho_s / r^4$]. Note that $g(r) > 0$. The scalar invariant \mathcal{R} is given by

$$\mathcal{R} = \frac{r_+ r_- [2r^2 - 6r_+ r + 3r_- r_+]}{2r^4 [(r - r_+)^2 + r_+(r_- - r_+)]}, \quad r_- > r_+, \tag{32}$$

and the Kretschmann scalar \mathcal{K} by

$$\mathcal{K} = \frac{\text{polynomial in } r^6}{r^8 [(r - r_+)^2 + r_+(r_- - r_+)]^2}, \quad r_- > r_+. \tag{33}$$

In the empty region $0 < r < r_-$, the solution is the Schwarzschild BH. Thus, the piecewise solution, $(f_{\text{BH}}(r), g_{\text{BH}}(r))$, given by

$$f_{\text{BH}}(r) = \begin{cases} f_0 \left(1 - \frac{r_+}{r}\right) & 0 < r < r_- \\ f(r) \text{ as given in (31)} & r \geq r_- \end{cases}, \quad (34)$$

$$g_{\text{BH}}(r) = \begin{cases} 1 - \frac{r_+}{r} & 0 < r < r_- \\ g(r) \text{ as given in (31)} & r \geq r_- \end{cases}, \quad (35)$$

is a Schwarzschild BH immersed in a DM Einstein cluster. The constant f_0 is such that

$$f_0 \sqrt{\frac{r_- r_+}{r_-}} = \exp \left\{ \sqrt{\frac{r_+}{r_- r_+}} \left[\arctan \left(\sqrt{\frac{r_- r_+}{r_+}} \right) - \frac{\pi}{2} \right] \right\}. \quad (36)$$

Finally, the radial pressure vanishes identically for all r and the tangential pressure is given by (29) for $r > r_-$. We conclude that the WEC is satisfied.

This piecewise structure leads to a qualitatively different dynamical behavior. Particle trajectories typically begin in a regular or quasi-regular regime at large radii and subsequently transition to chaotic motion as they approach the strong-field region. Chaotic behavior again manifests itself as a finite-time phenomenon, with trajectories ultimately crossing the event horizon after performing a variable number of loops around the black hole (see Fig. 7).

Notably, variations in the parameters of the Einstein cluster primarily affect the duration of the chaotic phase and the number of orbital revolutions preceding capture, while the overall qualitative features of the motion remain robust. This indicates that, in the presence of an event horizon, the global structure of the spacetime plays a dominant role in determining the fate of chaotic trajectories.

4. Physical interpretation

The configurations examined in this subsection reveal the interplay between horizon structure, matter distribution, and chaotic dynamics. In naked singularity spacetimes, the absence of a horizon allows chaotic motion to develop until direct capture by the singularity, whereas in Einstein-cluster configurations surrounding a black hole, the horizon enforces termination of the motion after a finite chaotic phase.

These results reinforce the picture that chaotic dynamics in dark-matter-embedded spacetimes is generically transient and strongly influenced by the global causal structure. At the same time, the detailed characteristics of chaos, such as its onset, duration, and phase-space morphology, remain sensitive to the presence or

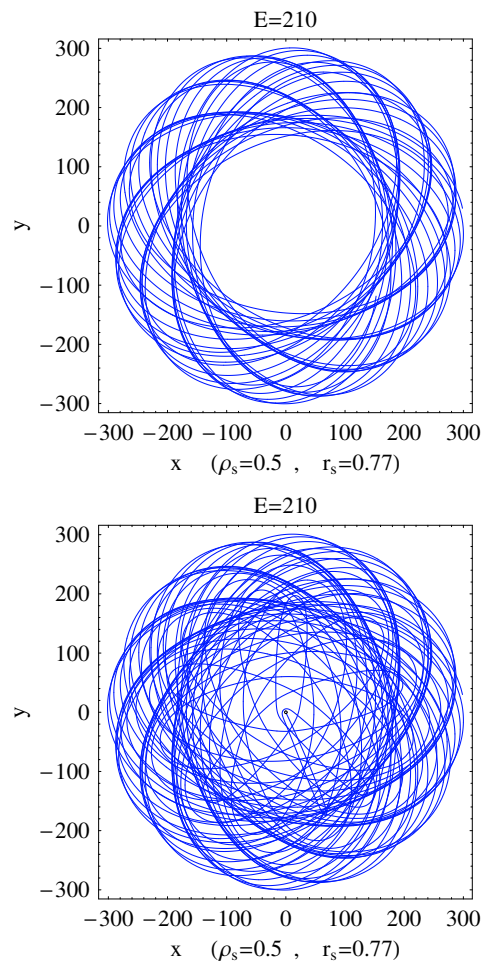


FIG. 7. Orbital projections onto the equatorial plane ($\theta = \pi/2$) in the spacetime defined by (34)-(35), corresponding to the case where the central mass equals the dark-matter mass contribution ($M = M_{\text{DM}}$). The parameters are $E = 210$, $\rho_s = 0.5$, $r_s = 0.77$, $r_+ = 2$, $r_- = 2.20873$, and initial radius $r(0) = 300$. Upper panel: Integration interval $0 \leq t \leq 5 \times 10^4$. Lower panel: Integration interval $0 \leq t \leq 7 \times 10^4$. Units $G = c = M = 1$ are adopted.

absence of horizons and to the internal matter distribution. These observations will be synthesized and compared across all geometries in the following subsection.

D. Universality and metric dependence of chaotic motion

Having analyzed chaotic dynamics across a broad class of dark-matter-embedded spacetimes, we can now distinguish between features that are genuinely universal and those that depend on the specific geometric realization of the central configuration. This comparative perspective allows us to separate structural properties of environmentally perturbed EMRIs from model-dependent effects tied to horizon structure and internal geometry.

A first robust conclusion is that chaos emerges gener-

TABLE I. Qualitative comparison of chaotic dynamics in dark-matter-embedded spacetimes.

Spacetime type	Horizon	Central structure	Chaos duration	Termination mechanism
Singular black hole	Yes	Curvature singularity	Finite-time	Horizon crossing
Regular black hole	Yes / No	Regular core	Extended finite-time	Horizon crossing (if present)
Naked singularity	No	Curvature singularity	Finite-time	Direct capture
Einstein cluster + BH	Yes	Matter-supported core	Finite-time	Horizon crossing

ically once integrability is broken in the strong-field regime. In all configurations examined, i.e. singular black holes, regular black holes, naked singularities, and Einstein-cluster spacetimes, the combined effect of strong gravity and environmental perturbations produces irregular orbital projections and stochastic Poincaré sections, according to the diagnostics introduced in Section III. This demonstrates that chaotic behavior is not an artifact of a particular metric choice, but a structural consequence of non-integrable EMRI dynamics in non-vacuum environments.

At the same time, the detailed manifestation of chaos depends sensitively on global and internal geometric properties. In singular black-hole geometries, the presence of an event horizon and a central curvature singularity renders chaos intrinsically finite in duration, as trajectories inevitably terminate in capture after a transient chaotic phase. Regular black holes modify this picture by eliminating the central singularity, allowing chaotic motion to persist for longer intervals and producing smoother transitions between regular and chaotic regimes. In naked-singularity configurations, chaotic motion may develop until direct capture by the singularity, whereas in Einstein-cluster configurations surrounding a black hole, the horizon again enforces termination after a finite chaotic episode. Thus, while the *existence* of chaos is robust, its *lifetime and dynamical morphology* are controlled by the underlying spacetime structure.

Dark-matter parameters further modulate the onset and extent of chaotic behavior. Changes in the scale radius and density primarily affect the energy threshold for chaos, the duration of the chaotic phase, and the degree of phase-space mixing. However, these variations do not alter the qualitative character of chaos itself, which remains strongly associated with the strong-field region and typically exhibits finite-time behavior in geometries admitting capture.

The principal qualitative trends are summarized in Table I, which collects the common features and geometry-dependent differences identified across all cases. Overall, our analysis establishes chaotic dynamics in dark-matter-embedded EMRIs as a structurally robust phenomenon, while demonstrating that its detailed imprint encodes information about horizon structure, core regularization, and matter distribution. This unified perspective provides the conceptual connection to the gravitational-wave signatures examined in the next section.

V. GRAVITATIONAL-WAVE SIGNATURES OF CHAOTIC EMRIS

Having established the dynamical properties of chaotic motion across a broad class of dark-matter-embedded spacetimes, we now proceed to the corresponding gravitational-wave signatures. Our aim in this section is not to assess detectability or to provide high-precision waveform modeling, but rather to identify robust qualitative imprints of chaotic dynamics on the emitted radiation. In this spirit, we adopt a simplified but physically transparent waveform construction that allows for a direct comparison between regular and chaotic orbital regimes.

The focus of the following analysis is therefore on how the loss of orbital regularity manifests itself in the time-domain structure and qualitative frequency content of gravitational-wave signals. By correlating features of the waveforms with the underlying phase-space dynamics discussed in the previous sections, we establish a clear connection between nonlinear orbital motion and gravitational-wave phenomenology in environmentally perturbed EMRIs.

A. Numerical Kludge waveform construction

In order to investigate the gravitational-wave signatures associated with chaotic dynamics, we use the numerical Kludge (NK) approach to waveform generation [103]. This method provides a computationally efficient framework for constructing approximate gravitational-wave signals from extreme mass-ratio inspirals, while retaining the essential features of the underlying orbital motion. The gravitational wave signals contain information about both chaotic and non-chaotic orbits due to EMRIs, therefore we are looking for any chaotic imprints considering different spacetimes.

Within the NK scheme, the trajectory of the small compact object is computed by solving the relativistic equations of motion in the curved background spacetime, as described in Sections II and IV. The resulting worldline is then interpreted as a source moving in flat spacetime, and the emitted gravitational radiation is calculated using the standard multipolar expansion of the gravitational field, typically at the quadrupole level. This hybrid procedure captures the dominant kinematical imprints of the motion on the waveform, while avoiding the technical complexity of fully rela-

tivistic waveform generation.

The numerical Kludge approach has been widely used in the literature as a qualitative tool for studying EMRI waveforms, particularly in contexts where the primary goal is to assess the impact of modifications to the orbital dynamics rather than to construct high-accuracy templates [70, 104, 105]. In the present work, this framework is especially well suited for isolating the effects of chaotic motion, since it allows for a direct comparison between waveforms generated by regular and chaotic trajectories under otherwise identical conditions.

It is important to emphasize that the NK waveforms employed here are not intended to provide faithful representations of signals detectable by future space-based observatories. Effects such as gravitational self-force, radiation reaction, and strong-field waveform corrections are neglected. Nevertheless, the NK approach is sufficient for identifying qualitative differences in waveform morphology and spectral content induced by chaotic dynamics, which is the primary focus of this study.

We assume that a test object of mass m orbits a gravitational source (either a black hole or a naked singularity) of mass M , where the test particle follows the geodesic motion. Under the assumption $M \gg m$, the quadrupole formula governing the emission of gravitational waves from the EMRI source is given by [70, 104, 105]

$$h_{ij} = \frac{4\eta M}{D_L} \left(v_i v_j - \frac{m}{r} n_i n_j \right), \quad (37)$$

where D_L is the luminosity distance of the EMRI system, $\eta = \frac{Mm}{(M+m)^2}$ represents the symmetric mass ratio, v_i denotes the i th component of the spatial velocity of the test particle, and n_i is the normalized unit vector pointing in the radial direction corresponding to the motion of the test particle.

The gravitational wave signal after projected onto the detector-adapted coordinate system, yields the corresponding plus h_+ and cross h_\times polarizations, given by [70]

$$h_+ = -\frac{2\eta}{D_L} \frac{M^2}{r} \left(1 + \cos^2 \iota \right) \cos(2\phi + 2\zeta), \quad (38)$$

$$h_\times = -\frac{4\eta}{D_L} \frac{M^2}{r} \cos \iota \sin(2\phi + 2\zeta), \quad (39)$$

where ι denotes the inclination angle between the orbital angular momentum of the EMRI system and the line of sight, while ζ represents the latitudinal angle. To illustrate the corresponding gravitational waveform of different regular and chaotic orbits, we implement them within different spacetimes in subsequent sections taking $\iota = \zeta = \pi/4$ and $D_L = 200$ Mpc ($M = 1 = c = G$ and $m = 10^{-5}$ as in the previous sections).

The waveforms presented in the following subsections are constructed directly from the numerically integrated orbital trajectories. Specifically, the equations of motion derived in Section II are solved in coordinate

time to obtain $r(t)$ and $\phi(t)$, from which the Cartesian trajectory is reconstructed in the equatorial plane. The gravitational radiation is then computed using the standard quadrupole formula within the numerical Kludge approximation, assuming a distant observer and neglecting radiation-reaction backreaction on the orbit. The $+$ and \times polarization modes are obtained from the second time derivatives of the mass quadrupole moment, and are plotted as functions of coordinate time in units where $G = c = 1$. This procedure ensures that differences between waveforms reflect purely dynamical effects associated with regular or chaotic motion.

B. Waveforms from regular and chaotic orbits

We now examine the gravitational-wave signals generated by regular and chaotic orbital motion, focusing on a direct qualitative comparison between the two regimes. In all cases, the waveforms are constructed using the numerical Kludge approach described in the previous subsection, and we consider the plus and cross polarizations, $h_+(t)$ and $h_\times(t)$, as representative observables (see Figs. 8, 9, 10) and 11).

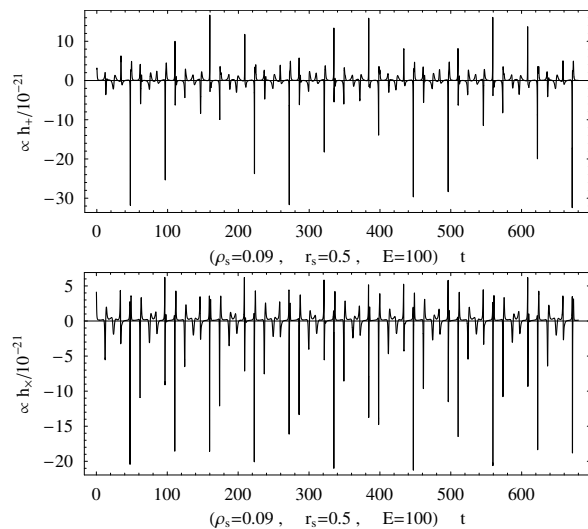


FIG. 8. Gravitational-wave signals generated in the regular (non-chaotic) regime for $E = 100$, $r_s = 0.5$, and $\rho_s = 0.09$, corresponding to the upper panel of Fig. 1 for metric (19). The waveforms exhibit smooth and quasi-periodic amplitude modulation, reflecting the underlying regular orbital motion. Upper panel: h_+ . Lower panel: h_\times . Time t is measured in units of M .

For a given background spacetime and fixed external-force parameters, pairs of trajectories are selected such that one exhibits regular motion while the other displays chaotic behavior, according to the diagnostics introduced in Section III. All remaining parameters are kept identical, ensuring that differences in the resulting waveforms can be attributed directly to the nature of the underlying dynamics.

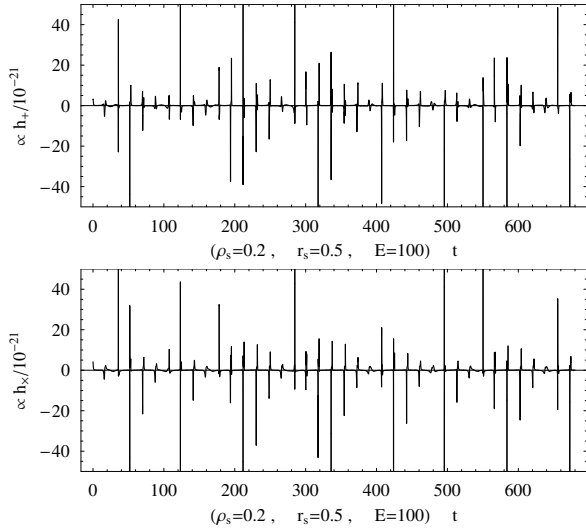


FIG. 9. Gravitational-wave signals in the chaotic regime for $E = 100$, $r_s = 0.5$, and $\rho_s = 0.2$, corresponding to the lower panel of Fig. 1 for metric (19). In contrast to the regular case of Fig. 8, the waveforms display irregular amplitude modulation and loss of quasi-periodic structure, reflecting the stochastic nature of the underlying orbital dynamics. Upper panel: h_+ . Lower panel: h_x . Time t is measured in units of M .

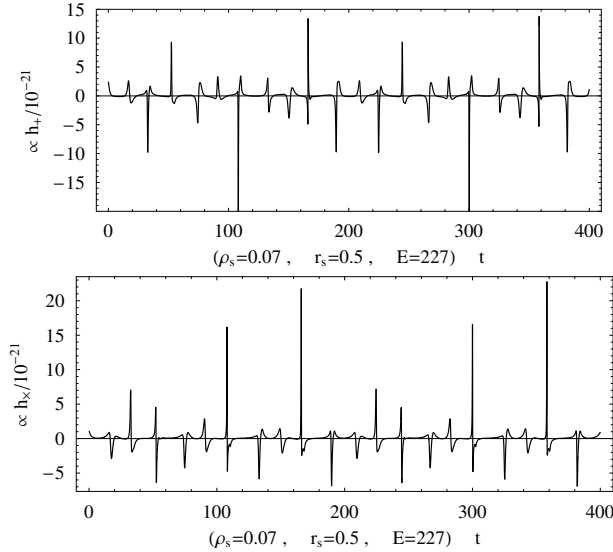


FIG. 10. Gravitational-wave signals for $E = 227$, $\rho_s = 0.07$, and $r_s = 0.5$, associated with metric (21) and corresponding to Fig. 2, shown during the early evolution phase $0 \leq t \leq 400$ (in units of M). In this interval the motion remains nearly regular, and the waveforms exhibit smooth and quasi-periodic amplitude modulation. Upper panel: h_+ . Lower panel: h_x .

In the regular regime, the gravitational-wave signals are characterized by a high degree of coherence. Both polarizations exhibit quasi-periodic oscillations with smoothly varying amplitudes and well-defined phase evolution. The waveform morphology closely reflects

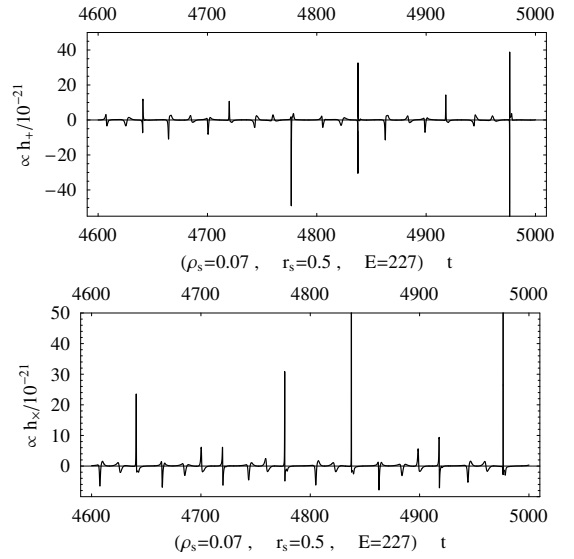


FIG. 11. Gravitational-wave signals for $E = 227$, $\rho_s = 0.07$, and $r_s = 0.5$, associated with metric (21) and corresponding to Fig. 2, shown during the late evolution phase $4600 \leq t \leq 5000$ (in units of M). In this interval the motion has entered a chaotic regime, and the waveforms display irregular amplitude modulation and loss of phase coherence compared to the early-time behavior shown in Fig. 10. Upper panel: h_+ . Lower panel: h_x .

the regularity of the orbital motion, with repeating patterns that persist throughout the evolution until termination.

In contrast, waveforms generated by chaotic trajectories display markedly different features. As the motion enters the chaotic phase, the gravitational-wave signal develops irregular amplitude modulation and a less uniform phase evolution. The loss of orbital coherence manifests itself as a distortion of the otherwise regular oscillatory pattern, with fluctuations that vary on multiple timescales. These effects become increasingly pronounced as the chaotic behavior intensifies.

In configurations where the orbital dynamics transitions from an initially regular phase to a chaotic one, the corresponding gravitational-wave signal exhibits a clear temporal change in character. During the early, quasi-regular stage, the waveform resembles that of a purely regular orbit, while in the later stages it acquires the irregular features associated with chaotic motion. This temporal correspondence provides a direct mapping between the dynamical evolution of the system and the morphology of the emitted gravitational radiation.

These qualitative differences between regular and chaotic waveforms are observed across all spacetime geometries considered in this work, including singular black holes, regular black holes, and naked-singularity or Einstein-cluster configurations. While the detailed waveform structure depends on the specific background and parameter choices, the contrast between coherent, quasi-periodic signals and irregular, modulated ones

emerges as a robust signature of chaotic dynamics.

C. Observable imprints of chaos

We now combine the main observable features imprinted by chaotic dynamics on the gravitational-wave signals of extreme mass-ratio inspirals. Although the waveforms discussed in the previous subsection are constructed using approximate methods, they nonetheless allow for the identification of robust qualitative signatures associated with the loss of orbital regularity.

A primary manifestation of chaotic motion in the gravitational-wave signal is the appearance of irregular amplitude modulation. While regular or quasi-regular orbits generate waveforms with smoothly varying and predictable amplitudes, chaotic trajectories induce fluctuations that vary erratically in time and lack a single dominant modulation scale. These amplitude variations reflect the sensitive dependence of the orbital motion on initial conditions and the resulting irregular evolution of the source's quadrupole moment.

A second characteristic imprint of chaos is spectral broadening. In regular regimes, the gravitational-wave signal is dominated by a discrete set of frequencies associated with the fundamental orbital timescales and their harmonics. As the motion becomes chaotic, this discrete spectral structure is progressively replaced by a broader frequency content, indicative of the excitation of multiple competing dynamical timescales. Although a detailed spectral analysis lies beyond the scope of the present work, this qualitative broadening emerges consistently across the chaotic configurations examined.

An important aspect of the systems considered here is that chaotic behavior is generically finite in duration. In spacetimes containing an event horizon or a naked singularity, chaotic motion typically develops in the strong-field region but eventually terminates when the orbiting object is captured. As a result, the associated gravitational-wave signatures of chaos are transient, appearing only during a limited segment of the inspiral. This finite-time nature of chaos distinguishes these systems from idealized models exhibiting sustained chaotic behavior and has direct implications for observational prospects.

From a detectability standpoint, the transient and parameter-dependent character of chaotic imprints suggests that their identification in realistic gravitational-wave data will be challenging. Nevertheless, the qualitative features identified here, i.e. irregular amplitude modulation and enhanced spectral complexity, may serve as indicators of non-integrable dynamics in EMRIs embedded in non-vacuum environments. Future studies incorporating more accurate waveform modeling and data-analysis techniques will be required to assess whether such signatures can be isolated in practice.

Overall, while the present analysis does not aim to establish chaos as an observable diagnostic in

gravitational-wave astronomy, it demonstrates that chaotic dynamics leave systematic and interpretable imprints on the emitted radiation. These findings provide a conceptual link between nonlinear orbital dynamics and gravitational-wave phenomenology, and motivate further investigation within more realistic modeling frameworks.

In the following we discuss the imprints of chaos as the massive particle m moves in the four geometries described by the metrics (19), (21), (22), and (27)-(31) under the effect of the effective harmonic potentials given in (7). The qualitative features discussed above manifest themselves consistently across the different space-time geometries examined in this work, albeit with distinct emphases depending on the underlying gravitational and environmental structure.

In dark-matter-embedded singular black-hole configurations of the Zhao type, regular and chaotic orbital regimes give rise to clearly distinguishable gravitational-wave morphologies. Regular motion produces coherent $+$ and \times polarizations with smoothly varying amplitudes, whereas chaotic motion induces irregular amplitude modulation and loss of phase coherence. The contrast between these regimes is particularly transparent when background parameters are held fixed and only the dynamical character of the orbit is altered.

For Bronnikov-type singular configurations, the gravitational-wave signal reflects the transitional nature of the orbital dynamics. During early stages, when the motion remains quasi-regular, the waveform closely resembles that of a regular inspiral. As the orbit enters a chaotic phase in the strong-field region, the signal develops irregular amplitude variations and enhanced complexity, before terminating when the particle is captured by the singularity. This temporal correspondence directly maps the onset of chaos in phase space to distinct changes in waveform morphology.

Regular black holes of the Simpson-Visser type exhibit a markedly different behavior. Owing to the absence of a central curvature singularity, chaotic motion develops more gradually and typically over much longer integration times. As a result, the associated gravitational-wave signatures remain largely coherent for extended periods, with only mild indications of irregularity at lower energies. Increasing the orbital energy enhances the degree of non-integrability and leads to progressively more pronounced deviations from regular waveform patterns, highlighting the stabilizing role of core regularization.

In naked-singularity and Einstein-cluster configurations, chaotic motion is again intrinsically finite in duration. The gravitational-wave signal displays irregular modulation during the chaotic phase, followed by abrupt termination as the particle is either captured by the naked singularity or crosses the event horizon in the black-hole case. Variations in the dark-matter scale primarily affect the duration and intensity of the chaotic phase, while the qualitative structure of the waveform

imprints remains robust.

Taken together, these results demonstrate that while the detailed appearance of gravitational-wave signals depends on the specific spacetime geometry, the qualitative imprints of chaotic dynamics, such as irregular amplitude modulation, enhanced spectral complexity, and transient behavior, are generic. The precise manifestation of these features encodes information about the presence of horizons, core regularization, and environmental matter distributions, thereby providing a direct conceptual link between nonlinear orbital dynamics and gravitational-wave phenomenology.

VI. CONCLUSIONS

In this work we have investigated the emergence and physical implications of chaotic dynamics in extreme mass-ratio inspirals evolving in dark-matter-embedded spacetimes. Motivated by growing astrophysical evidence that supermassive black holes are surrounded by non-negligible matter distributions, and by earlier indications that environmental perturbations can induce non-integrable orbital dynamics, our objective was twofold: first, to assess the robustness of chaotic motion across a broad class of spacetime geometries, and second, to determine whether such dynamics leave systematic imprints on the emitted gravitational radiation.

To this end, we developed a unified dynamical framework for test-particle motion in spherically symmetric spacetimes, employing horizon-regular coordinates that enable a consistent treatment of singular black holes, regular compact objects, naked singularities, and Einstein-cluster configurations within a single formalism. Environmental effects were modeled through effective harmonic perturbations, providing a controlled mechanism for breaking integrability while isolating qualitative dynamical features. Chaotic behavior was identified using complementary diagnostics, including orbital projections and Poincaré sections, with particular attention to the finite-time character of chaos in strong-field relativistic systems.

Our analysis demonstrates that chaotic dynamics is not an artifact of a particular metric realization, but rather a generic consequence of environmentally perturbed EMRIs once the motion enters the strong-field regime. Across all configurations considered, such as singular black holes, regular black holes, naked singularities, and Einstein-cluster geometries, chaos emerges when integrability is sufficiently broken. At the same time, its detailed manifestation depends sensitively on the global and internal structure of the spacetime. In singular black-hole geometries, the presence of an event horizon and a curvature singularity enforces finite-time chaos, with trajectories ultimately terminating after a transient chaotic phase. Regular black holes modify this picture by removing the central singularity, thereby allowing chaotic dynamics to persist over longer intervals

and smoothing the transition from regular to chaotic motion. Horizonless configurations exhibit chaotic behavior until direct capture, while Einstein-cluster geometries again display finite-time chaos governed by horizon crossing.

We further examined the gravitational-wave signatures associated with these dynamical regimes using the numerical Kludge approach. Although approximate, this framework suffices to reveal robust qualitative distinctions between waveforms generated by regular and chaotic trajectories. Chaotic motion consistently induces irregular amplitude modulation, loss of phase coherence, and spectral broadening, in contrast to the smooth and quasi-periodic signals produced by regular orbits. In systems exhibiting a transition from regular to chaotic dynamics, the gravitational-wave signal mirrors this evolution, developing irregular features precisely when chaos sets in phase space. These imprints appear across all spacetime geometries considered, while their duration and intensity encode information about horizon structure, core regularization, and the dark-matter distribution.

The central conclusion of this work is therefore twofold. First, chaotic dynamics in EMRIs embedded in dark-matter environments is a robust and generic strong-field phenomenon. Second, although chaos is typically finite in duration, it leaves systematic and physically interpretable imprints on the gravitational radiation, establishing a conceptual bridge between nonlinear orbital dynamics and gravitational-wave phenomenology. While the detectability of such signatures in realistic data remains to be quantified, their consistent appearance across disparate geometries underscores their physical relevance.

For comparison with the recent works by Das et al. [41, 42], which analyze chaotic dynamics and gravitational-wave signatures in a Schwarzschild-like black hole embedded in a Dehnen-type dark-matter halo at leading order, our study introduces several extensions. First, we derive and employ an exact black-hole solution associated with the more general Zhao density profile, of which the Dehnen profile constitutes a special case, thus allowing a consistent treatment of the full metric structure without reliance on leading-order approximations. Second, whereas Refs. [41, 42] focus exclusively on singular Schwarzschild-like geometries, we perform a systematic comparative analysis across singular black holes, regular black holes, naked singularities, and Einstein-cluster configurations (derived in this work). This broader framework enables us to disentangle universal features of environmentally induced chaos from those that depend sensitively on horizon structure, singularity properties, and core regularization. In this way, the present work generalizes previous findings and provides a unified perspective on chaotic dynamics and their gravitational-wave imprints in dark-matter-embedded compact-object spacetimes.

Several directions for future investigation naturally

follow. Incorporating radiation reaction and self-force effects would clarify the interplay between dissipation and chaos, and determine whether chaotic behavior is enhanced, suppressed, or qualitatively altered during realistic inspirals. More accurate waveform modeling, combined with dedicated data-analysis strategies, will be necessary to assess the observational prospects for detecting chaotic imprints with space-based observatories such as LISA. Extending the present framework to rotating spacetimes and more realistic environmental models represents an essential step toward establishing the full astrophysical relevance of chaotic dynamics in extreme mass-ratio inspirals. These investigations are left for future projects.

ACKNOWLEDGMENTS

E.N.S. gratefully acknowledges the contribution of the LISA Cosmology Working Group (CosWG), as well as support from the COST Actions CA21136 - Addressing observational tensions in cosmology with systematics and fundamental physics (CosmoVerse) - CA23130, Bridging high and low energies in search of quantum gravity (BridgeQG) and CA21106 - COSMIC WISPerS in the Dark Universe: Theory, astrophysics and experiments (CosmicWISPerS).

Appendix A: Derivation of metric (19)

In this Appendix we outline the derivation of the spacetime metric (19) sourced by the Zhao-type dark-matter density profile introduced in the main text. We work within general relativity and assume a static, spherically symmetric geometry supported by an anisotropic matter distribution,

$$T^{\mu}_{\nu} = \text{diag}(-c^2\rho, p_r, p_t, p_t), \quad (\text{A.1})$$

where $p_r \neq p_t$ in general, as is natural for halo-like configurations. The metric is written in terms of a mass function $m(r)$ defined through $g(r) = 1 - 2Gm(r)/(c^2r)$, and related to the energy density via

$$\rho(r) = \frac{m'(r)}{4\pi r^2}. \quad (\text{A.2})$$

The (t, t) component of the Einstein field equations ($G_{\mu\nu} = \kappa T_{\mu\nu}$, $\kappa \equiv 8\pi G/c^4$) determines the mass function. Integrating the corresponding equation for the density profile considered in the main text yields

$$m(r) = M - \frac{2\pi r_s^4 \rho_s r}{r^2 + r_s^2} + 2\pi r_s^3 \rho_s \arctan\left(\frac{r}{r_s}\right), \quad (\text{A.3})$$

where M denotes the asymptotic mass of the central object. Substituting this expression into the metric ansatz

leads to the lapse function

$$f(r) = 1 - \frac{2GM}{c^2 r} + \frac{4\pi G r_s^4 \rho_s}{c^2 (r^2 + r_s^2)} - \frac{4\pi G r_s^3 \rho_s}{c^2 r} \arctan\left(\frac{r}{r_s}\right). \quad (\text{A.4})$$

The remaining independent components of the field equations determine the radial and tangential pressures. From the (r, r) equation we obtain

$$p_r(r) = -c^2 \rho(r) = -\frac{c^2 r_s^4 \rho_s}{(r^2 + r_s^2)^2}, \quad (\text{A.5})$$

while the (θ, θ) component yields

$$p_t(r) = -\frac{Gm''(r)}{c^2 r} = \frac{c^2 r_s^4 \rho_s (r^2 - r_s^2)}{(r^2 + r_s^2)^3}. \quad (\text{A.6})$$

The stress tensor is therefore anisotropic but completely determined by the chosen density profile.

Finally, we verify that the weak energy condition (WEC) is satisfied throughout the spacetime. The energy density is manifestly positive,

$$\rho(r) = \frac{r_s^4 \rho_s}{(r^2 + r_s^2)^2} > 0, \quad (\text{A.7})$$

and one finds

$$\rho(r) + \frac{p_r}{c^2} = 0, \quad (\text{A.8})$$

$$\rho(r) + \frac{p_t}{c^2} = \frac{2r_s^4 \rho_s r^2}{(r^2 + r_s^2)^3} > 0. \quad (\text{A.9})$$

Hence the matter configuration sourcing metric (19) satisfies the weak energy condition everywhere and is therefore physically admissible.

Appendix B: Derivation of metrics (27) and (31)

In this Appendix we outline the construction of the metrics (27) and (31), which describe a dark-matter-supported Einstein-cluster configuration surrounding a central compact object. We consider the general static, spherically symmetric line element

$$ds^2 = -c^2 f(r) dt^2 + \frac{dr^2}{1 - \frac{2Gm(r)}{c^2 r}} + r^2 d\Omega^2, \quad (\text{B.1})$$

where the mass function $m(r)$ is defined through $g(r) = 1 - 2Gm(r)/(c^2 r)$, and we assume an anisotropic effective fluid

$$T^{\mu}_{\nu} = \text{diag}(-c^2\rho, p_r, p_t, p_t). \quad (\text{B.2})$$

We are interested in a configuration with density profile $\rho \propto r^{-4}$, which yields an Einstein cluster when the

radial pressure vanishes identically. Accordingly, we prescribe the mass function

$$m(r) = c_1 - \frac{4\pi r_s^4 \rho_s}{r}, \quad (r_{\min} \leq r < \infty), \quad (\text{B.3})$$

where r_s is a scale parameter, ρ_s sets the density scale, and the constant c_1 will be fixed by the asymptotic mass content (central object plus dark matter).

The (t, t) field equation yields the energy density

$$\rho(r) = \frac{m'(r)}{4\pi r^2} = \frac{r_s^4 \rho_s}{r^4}, \quad (\text{B.4})$$

while the (r, r) component gives the radial pressure in terms of $f(r)$ and $m(r)$ as

$$\kappa p_r = \frac{c^2 r - 2Gm(r)}{c^2 r^2} \frac{f'(r)}{f(r)} - \frac{2Gm(r)}{c^2 r^3}. \quad (\text{B.5})$$

An Einstein-cluster configuration corresponds to $p_r \equiv 0$. Integrating (B.5) under this condition yields

$$f(r) = \left(\sqrt{\frac{r-r_+}{r-r_-}} \right)^{c_2} \frac{\sqrt{(r-r_+)(r-r_-)}}{r}, \quad (\text{B.6})$$

where the second factor is $\sqrt{g(r)}$, and c_2 is an integration constant given by

$$c_2 = \frac{1}{\sqrt{1 - \frac{8\pi c^2 r_s^4 \rho_s}{c_1^2 G}}}. \quad (\text{B.7})$$

The parameters r_{\pm} are the (real) roots associated with $g(r)$,

$$r_{\pm} = \frac{c_1 G \pm \sqrt{G(c_1^2 G - 8\pi c^2 r_s^4 \rho_s)}}{c^2}, \quad (\text{B.8})$$

and the physical character of the solution depends on the ordering of these two scales, as discussed below.

a. Case $r_-/r_+ < 1$

In this case the dark-matter distribution is taken to extend from $r = r_+$ to spatial infinity. The total dark-

matter mass contribution is

$$\int_{r_+}^{\infty} 4\pi r^2 \rho(r) dr = \int_{r_+}^{\infty} \frac{4\pi r_s^4 \rho_s}{r^2} dr = \frac{c^2}{2G} r_-. \quad (\text{B.9})$$

Denoting by M the central mass parameter, we fix c_1 by requiring that the asymptotic mass equals the sum of the central contribution plus the dark-matter mass. Solving $c_1 = M + c^2 r_- / (2G)$ gives

$$c_1 = M \left(1 + \frac{2\pi c^2 r_s^4 \rho_s}{GM^2} \right). \quad (\text{B.10})$$

With this identification, the metric functions $f(r)$ and $g(r)$ reduce to the expressions presented in (27), and the corresponding spacetime describes a naked singularity located at $r = r_+$, surrounded by a dark-matter Einstein cluster.

b. Case $r_-/r_+ > 1$

When $r_- > r_+$, it is natural to consider the dark-matter distribution as extending from $r = r_-$ outwards. In this case the mass contribution of the cluster becomes

$$\int_{r_-}^{\infty} 4\pi r^2 \rho(r) dr = \int_{r_-}^{\infty} \frac{4\pi r_s^4 \rho_s}{r^2} dr = \frac{4\pi r_s^4 \rho_s}{r_-} = M, \quad (\text{B.11})$$

which implies $c_1 = 2M$ and hence $m(r) = 2M - Mr_-/r$. Integrating (B.5) again under $p_r \equiv 0$ yields the metric functions given in (31). In this case the region $0 < r < r_-$ is vacuum Schwarzschild, while for $r \geq r_-$ the solution describes a Schwarzschild black hole immersed in an Einstein-cluster dark-matter distribution.

For completeness, we note that if one were to evaluate the dark-matter mass by integrating from r_+ instead of r_- in the regime $r_- > r_+$, one would be led to a naked-singularity-type solution that is not physically appropriate in the intermediate region $r_+ < r < r_-$.

-
- [1] B. P. Abbott *et al.* [LIGO Scientific and Virgo], Phys. Rev. Lett. **116**, no.6, 061102 (2016) [[arXiv:1602.03837 \[gr-qc\]](#)].
- [2] B. P. Abbott *et al.* [LIGO Scientific and Virgo], Phys. Rev. X **9**, no.3, 031040 (2019) [[arXiv:1811.12907 \[astro-ph.HE\]](#)].
- [3] P. Amaro-Seoane *et al.* [LISA], [[arXiv:1702.00786 \[astro-ph.IM\]](#)].
- [4] J. Luo *et al.* [TianQin], Class. Quant. Grav. **33**, no.3, 035010 (2016) [[arXiv:1512.02076 \[astro-ph.IM\]](#)].
- [5] W. H. Ruan, Z. K. Guo, R. G. Cai and Y. Z. Zhang, Int. J. Mod. Phys. A **35**, no.17, 2050075 (2020) [[arXiv:1807.09495 \[gr-qc\]](#)].
- [6] L. Barack, V. Cardoso, S. Nissanke, T. P. Sotiriou, A. Askar, C. Belczynski, G. Bertone, E. Bon, D. Blas and R. Brito, *et al.* Class. Quant. Grav. **36**, no.14, 143001 (2019) [[arXiv:1806.05195 \[gr-qc\]](#)].

- [7] F. D. Ryan, Phys. Rev. D **52**, 5707-5718 (1995) [[No arXiv entry](#)].
- [8] K. Glampedakis and S. Babak, Class. Quant. Grav. **23**, 4167-4188 (2006) [[arXiv:gr-qc/0510057 \[gr-qc\]](#)].
- [9] N. Yunes and L. C. Stein, Phys. Rev. D **83**, 104002 (2011) [[arXiv:1101.2921 \[gr-qc\]](#)].
- [10] E. Berti *et al.*, Class. Quant. Grav. **32**, 243001 (2015) [[arXiv:1501.07274 \[gr-qc\]](#)].
- [11] E. N. Saridakis *et al.*, *Modified Gravity and Cosmology. An Update by the CANTATA Network*, Springer, (2021), [[arXiv:2105.12582 \[gr-qc\]](#)].
- [12] B. Kocsis, N. Yunes and A. Loeb, Phys. Rev. D **84**, 024032 (2011) [[arXiv:1104.2322 \[astro-ph.GA\]](#)].
- [13] E. Barausse, V. Cardoso and P. Pani, Phys. Rev. D **89**, no.10, 104059 (2014) [[arXiv:1404.7149 \[gr-qc\]](#)].
- [14] R. Narayan, New J. Phys. **7**, 199 (2005) [[arXiv:gr-qc/0506078 \[gr-qc\]](#)].
- [15] D. Merritt, *Dynamics and Evolution of Galactic Nuclei*, Princeton University Press (2013).
- [16] R. Blandford, D. Meier and A. Readhead, Ann. Rev. Astron. Astrophys. **57**, 467-509 (2019) [[arXiv:1812.06025 \[astro-ph.HE\]](#)].
- [17] G. Bertone, D. Hooper and J. Silk, Phys. Rept. **405**, 279-390 (2005) [[arXiv:hep-ph/0404175 \[hep-ph\]](#)].
- [18] O. Y. Gnedin and J. R. Primack, Phys. Rev. Lett. **93**, 061302 (2004) [[arXiv:astro-ph/0308385 \[astro-ph\]](#)].
- [19] N. J. Cornish and J. J. Levin, Phys. Rev. D **55**, 7489-7510 (1997) [[arXiv:gr-qc/9612066 \[gr-qc\]](#)].
- [20] J. J. Levin, Phys. Rev. Lett. **84**, 3515 (2000) [[arXiv:gr-qc/9910040 \[gr-qc\]](#)].
- [21] G. Contopoulos, *Order and Chaos in Dynamical Astronomy*, Springer (2002).
- [22] J. D. Schnittman, A. Buonanno, J. R. van Meter, J. G. Baker, W. D. Boggs, J. Centrella, B. J. Kelly and S. T. McWilliams, Phys. Rev. D **77**, 044031 (2008) [[arXiv:0707.0301 \[gr-qc\]](#)].
- [23] O. Semerak and P. Sukova, Mon. Not. Roy. Astron. Soc. **404**, 545-574 (2010) [[arXiv:1211.4106 \[gr-qc\]](#)].
- [24] A. M. Ghez, S. Salim, N. N. Weinberg, J. R. Lu, T. Do, J. K. Dunn, K. Matthews, M. Morris, S. Yelda and E. E. Becklin, *et al.* Astrophys. J. **689**, 1044-1062 (2008) [[arXiv:0808.2870 \[astro-ph\]](#)].
- [25] R. Schoedel, D. Merritt and A. Eckart, Astron. Astrophys. **502**, 91 (2009) [[arXiv:0902.3892 \[astro-ph.GA\]](#)].
- [26] M. Rizwan, M. Jamil and M. Z. A. Moughal, Eur. Phys. J. C **85**, no.3, 359 (2025) [[arXiv:2501.04739 \[gr-qc\]](#)].
- [27] M. Cruz, A. Ganguly, R. Gannouji, G. Leon and E. N. Saridakis, Class. Quant. Grav. **34**, no.12, 125014 (2017) [[arXiv:1702.01754 \[gr-qc\]](#)].
- [28] M. Rizwan, M. Jamil and K. Jusufi, Phys. Rev. D **99**, no.2, 024050 (2019) [[arXiv:1812.01331 \[gr-qc\]](#)].
- [29] S. H. Hendi, A. Nemati, K. Lin and M. Jamil, Eur. Phys. J. C **80**, no.4, 296 (2020) [[arXiv:2001.01591 \[gr-qc\]](#)].
- [30] K. Jusufi, M. Jamil and T. Zhu, Eur. Phys. J. C **80**, no.5, 354 (2020) [[arXiv:2005.05299 \[gr-qc\]](#)].
- [31] J. Rayimbaev, S. Shaymatov and M. Jamil, Eur. Phys. J. C **81**, no.8, 699 (2021) [[arXiv:2107.13436 \[gr-qc\]](#)].
- [32] S. Nampalliwar, S. Kumar, K. Jusufi, Q. Wu, M. Jamil and P. Salucci, Astrophys. J. **916**, no.2, 116 (2021) [[arXiv:2103.12439 \[astro-ph.HE\]](#)].
- [33] P. Mach and A. Odrzywo, Phys. Rev. Lett. **126**, no.10, 101104 (2021) [[arXiv:2103.03595 \[gr-qc\]](#)].
- [34] E. González, K. Jusufi, G. Leon and E. N. Saridakis, Phys. Dark Univ. **42**, 101304 (2023) [[arXiv:2305.14305 \[astro-ph.CO\]](#)].
- [35] S. Yang, Y. P. Zhang, T. Zhu, L. Zhao and Y. X. Liu, JCAP **01**, 091 (2025) [[arXiv:2407.00283 \[gr-qc\]](#)].
- [36] A. Al-Badawi and S. Shaymatov, Chin. Phys. C **49**, no.5, 055101 (2025) [[arXiv:2501.15397 \[gr-qc\]](#)].
- [37] F. F. Santos, B. Pourhassan and E. N. Saridakis, [[arXiv:2509.23430 \[hep-th\]](#)].
- [38] A. Anand, S. Devdutt, K. Jusufi and E. N. Saridakis, [[arXiv:2511.04613 \[gr-qc\]](#)].
- [39] A. Anand, K. Jusufi, S. Basilakos and E. N. Saridakis, Eur. Phys. J. C **86**, no.2, 126 (2026) [[arXiv:2512.13769 \[gr-qc\]](#)].
- [40] K. Nozari, M. Hajebrahimi, S. Saghafi, G. Mustafa and E. N. Saridakis, [[arXiv:2602.16237 \[gr-qc\]](#)].
- [41] S. Das, S. Dalui, B. H. Lee and Y. F. Cai, [[arXiv:2511.03657 \[gr-qc\]](#)].
- [42] S. Das, S. Dalui, B. H. Lee and Y. F. Cai, [[arXiv:2512.04848 \[gr-qc\]](#)].
- [43] N. J. Cornish and J. J. Levin, Phys. Rev. D **68**, 024004 (2003) [[arXiv:astro-ph/0305410 \[astro-ph\]](#)].
- [44] L. Bombelli and E. Calzetta, Class. Quant. Grav. **9**, 2573-2599 (1992).
- [45] Y. Sota, S. Suzuki and K. i. Maeda, Class. Quant. Grav. **13**, 1241-1260 (1996) [[arXiv:gr-qc/9505036 \[gr-qc\]](#)].
- [46] W. M. Vieira and P. S. Letelier, Phys. Rev. Lett. **76**, 1409-1412 (1996) [[arXiv:gr-qc/9604037 \[gr-qc\]](#)].
- [47] S. Suzuki and K. i. Maeda, Phys. Rev. D **55**, 4848-4859 (1997) [[arXiv:gr-qc/9604020 \[gr-qc\]](#)].
- [48] J. M. Aguirregabiria, Phys. Lett. A **224**, 234-238 (1997) [[arXiv:gr-qc/9604032 \[gr-qc\]](#)].
- [49] P. Breitenlohner, G. V. Lavrelashvili and D. Maison, Nucl. Phys. B **524**, 427-443 (1998) [[arXiv:gr-qc/9703047 \[gr-qc\]](#)].
- [50] W. Han, Gen. Rel. Grav. **40**, 1831-1847 (2008) [[arXiv:1006.2229 \[gr-qc\]](#)].
- [51] M. Takahashi and H. Koyama, Astrophys. J. **693**, 472-485 (2009) [[arXiv:0807.0277 \[astro-ph\]](#)].
- [52] J. L. F. Barbon and J. M. Magan, Phys. Rev. D **84**, 106012 (2011) [[arXiv:1105.2581 \[hep-th\]](#)].
- [53] M. Gaspari, M. Ruskowski and S. P. Oh, Mon. Not. Roy. Astron. Soc. **432**, 3401 (2013) [[arXiv:1301.3130 \[astro-ph.CO\]](#)].
- [54] V. Mewes, J. A. Font, F. Galeazzi, P. J. Montero and N. Stergioulas, Phys. Rev. D **93**, no.6, 064055 (2016) [[arXiv:1506.04056 \[gr-qc\]](#)].
- [55] P. V. P. Cunha, J. Grover, C. Herdeiro, E. Radu, H. Runarsson and A. Wittig, Phys. Rev. D **94**, no.10, 104023 (2016) [[arXiv:1609.01340 \[gr-qc\]](#)].
- [56] S. Chen, M. Wang and J. Jing, JHEP **09**, 082 (2016) [[arXiv:1604.02785 \[gr-qc\]](#)].
- [57] R. Pánis, M. Kološ and Z. Stuchlík, Eur. Phys. J. C **79**, no.6, 479 (2019) [[arXiv:1905.01186 \[gr-qc\]](#)].
- [58] V. De Falco and W. Borrelli, [[arXiv:2105.00965 \[gr-qc\]](#)].
- [59] Y. Zhao, X. Ren, A. Ilyas, E. N. Saridakis and Y. F. Cai, JCAP **10**, 087 (2022) [[arXiv:2204.11169 \[gr-qc\]](#)].
- [60] M. Wang, S. Chen and J. Jing, Commun. Theor. Phys. **74**, no.9, 097401 (2022) [[arXiv:2205.05855 \[gr-qc\]](#)].
- [61] J. Xie, Y. Wang and B. Tang, Phys. Dark Univ. **40**, 101184 (2023) [[arXiv:2210.08641 \[gr-qc\]](#)].
- [62] Y. Zhao, Y. Cai, S. Das, G. Lambiase, E. N. Saridakis and E. C. Vagenas, Nucl. Phys. B **1004**, 116545 (2024) [[arXiv:2301.09147 \[gr-qc\]](#)].
- [63] L. Yang and N. Engelhardt, JHEP **03**, 153 (2025) [[arXiv:2302.11013 \[hep-th\]](#)].

- [64] Z. Y. Tu, T. Zhu and A. Wang, Phys. Rev. D **108**, no.2, 2 (2023) [[arXiv:2304.14160 \[gr-qc\]](#)].
- [65] W. H. Wu, C. Y. Zhang, C. G. Shao and W. L. Qian, Chin. Phys. C **47**, no.8, 085102 (2023) [[arXiv:2303.04907 \[gr-qc\]](#)].
- [66] W. Cao, X. Wu and J. Lyu, Eur. Phys. J. C **84**, no.4, 435 (2024) [[arXiv:2404.19225 \[gr-qc\]](#)].
- [67] J. Lu and X. Wu, Universe **10**, no.7, 277 (2024) [[arXiv:2406.18943 \[gr-qc\]](#)].
- [68] F. d. Rodrigues, R. A. Mosna and R. S. S. Vieira, Gen. Rel. Grav. **56**, no.10, 112 (2024) [[arXiv:2409.14667 \[gr-qc\]](#)].
- [69] T. S. Amancio, R. A. Mosna and R. S. S. Vieira, Phys. Rev. D **110**, no.12, 124048 (2024) [[arXiv:2412.15938 \[gr-qc\]](#)].
- [70] O. Shabbir, M. Jamil and M. Azreg-Aïnou, Phys. Dark Univ. **47**, 101816 (2025) [[arXiv:2501.04367 \[gr-qc\]](#)].
- [71] H. Hadi, A. R. Akbarieh and E. N. Saridakis, Phys. Lett. B **867**, 139602 (2025) [[arXiv:2505.23226 \[gr-qc\]](#)].
- [72] A. Fayyaz, G. Abbas, M. Bin-Asfour and D. Chen, Phys. Lett. B **871**, 139965 (2025)
- [73] S. Dalui, C. Singha and K. Bhattacharya, Phys. Lett. B **874**, 140256 (2026) [[arXiv:2602.04423 \[gr-qc\]](#)].
- [74] T. Zahra, O. Shabbir, B. Majeed, M. Jamil, J. Rayimbaev and A. Shermatov, Eur. Phys. J. C **85**, no.11, 1340 (2025) [[arXiv:2510.22761 \[gr-qc\]](#)].
- [75] J. M. Bardeen, Proc. Int. Conf. GR5, Tbilisi (1968).
- [76] A. Borde, Phys. Rev. D **55**, 7615-7617 (1997) [[arXiv:gr-qc/9612057 \[gr-qc\]](#)].
- [77] A. Burinskii and S. R. Hildebrandt, Phys. Rev. D **65**, 104017 (2002) [[arXiv:hep-th/0202066 \[hep-th\]](#)].
- [78] S. A. Hayward, Phys. Rev. Lett. **96**, 031103 (2006) [[arXiv:gr-qc/0506126 \[gr-qc\]](#)].
- [79] W. Berej, J. Matyjasek, D. Tryniecki and M. Woronowicz, Gen. Rel. Grav. **38**, 885-906 (2006) [[arXiv:hep-th/0606185 \[hep-th\]](#)].
- [80] K. A. Bronnikov, V. N. Melnikov and H. Dehnen, Gen. Rel. Grav. **39**, 973-987 (2007) [[arXiv:gr-qc/0611022 \[gr-qc\]](#)].
- [81] J. P. S. Lemos and V. T. Zanchin, Phys. Rev. D **83**, 124005 (2011) [[arXiv:1104.4790 \[gr-qc\]](#)].
- [82] A. Flachi and J. P. S. Lemos, Phys. Rev. D **87**, no.2, 024034 (2013) [[arXiv:1211.6212 \[gr-qc\]](#)].
- [83] Z. Li and C. Bambi, JCAP **01**, 041 (2014) [[arXiv:1309.1606 \[gr-qc\]](#)].
- [84] C. Bambi and L. Modesto, Phys. Lett. B **721**, 329-334 (2013) [[arXiv:1302.6075 \[gr-qc\]](#)].
- [85] J. C. S. Neves and A. Saa, Phys. Lett. B **734**, 44-48 (2014) [[arXiv:1402.2694 \[gr-qc\]](#)].
- [86] Z. Y. Fan and X. Wang, Phys. Rev. D **94**, no.12, 124027 (2016) [[arXiv:1610.02636 \[gr-qc\]](#)].
- [87] A. Abdujabbarov, M. Amir, B. Ahmedov and S. G. Ghosh, Phys. Rev. D **93**, no.10, 104004 (2016) [[arXiv:1604.03809 \[gr-qc\]](#)].
- [88] B. Toshmatov, Z. Stuchlík and B. Ahmedov, Phys. Rev. D **95**, no.8, 084037 (2017) [[arXiv:1704.07300 \[gr-qc\]](#)].
- [89] K. Jusufi, A. Övgün, J. Saavedra, Y. Vásquez and P. A. González, Phys. Rev. D **97**, no.12, 124024 (2018) [[arXiv:1804.00643 \[gr-qc\]](#)].
- [90] R. Carballo-Rubio, F. Di Filippo, S. Liberati, C. Pacilio and M. Visser, JHEP **07**, 023 (2018) [[arXiv:1805.02675 \[gr-qc\]](#)].
- [91] A. Övgün, Phys. Rev. D **99**, no.10, 104075 (2019) [[arXiv:1902.04411 \[gr-qc\]](#)].
- [92] A. Simpson and M. Visser, Universe **6**, no.1, 8 (2019) [[arXiv:1911.01020 \[gr-qc\]](#)].
- [93] R. Kumar, S. G. Ghosh and A. Wang, Phys. Rev. D **100**, no.12, 124024 (2019) [[arXiv:1912.05154 \[gr-qc\]](#)].
- [94] K. Jusufi, Phys. Dark Univ. **39**, 101156 (2023) [[arXiv:2212.06760 \[gr-qc\]](#)].
- [95] C. Lan, H. Yang, Y. Guo and Y. G. Miao, Int. J. Theor. Phys. **62**, no.9, 202 (2023) [[arXiv:2303.11696 \[gr-qc\]](#)].
- [96] P. Bueno, P. A. Cano and R. A. Hennigar, Phys. Lett. B **861**, 139260 (2025) [[arXiv:2403.04827 \[gr-qc\]](#)].
- [97] I. Dymnikova, Class. Quant. Grav. **21**, 4417-4429 (2004) [[arXiv:gr-qc/0407072 \[gr-qc\]](#)].
- [98] K. A. Bronnikov and J. C. Fabris, Phys. Rev. Lett. **96**, 251101 (2006) [[arXiv:gr-qc/0511109 \[gr-qc\]](#)].
- [99] A. Simpson and M. Visser, JCAP **02**, 042 (2019) [[arXiv:1812.07114 \[gr-qc\]](#)].
- [100] H. Zhao, Mon. Not. Roy. Astron. Soc. **278**, 488-496 (1996) [[arXiv:astro-ph/9509122 \[astro-ph\]](#)].
- [101] L. Balart and E. C. Vagenas, Phys. Lett. B **730**, 14-17 (2014) [[arXiv:1401.2136 \[gr-qc\]](#)].
- [102] K. A. Bronnikov, Int. J. Mod. Phys. D **27**, no.06, 1841005 (2018) [[arXiv:1711.00087 \[gr-qc\]](#)].
- [103] S. Babak, H. Fang, J. R. Gair, K. Glampedakis and S. A. Hughes, Phys. Rev. D **75**, 024005 (2007) [erratum: Phys. Rev. D **77**, 04990 (2008)] [[arXiv:gr-qc/0607007 \[gr-qc\]](#)].
- [104] L. Zhao, M. Tang and Z. Xu, Eur. Phys. J. C **85**, no.1, 36 (2025) [[arXiv:2411.01979 \[gr-qc\]](#)].
- [105] T. Xamidov, S. Shaymatov, Q. Wu and T. Zhu, [[arXiv:2602.09453 \[gr-qc\]](#)].